SEISMIC INVESTIGATION OF THE MORPHOLOGY OF A TUNNEL CHANNEL OF THE GREEN BAY LOBE, WISCONSIN, USA

A Thesis
Submitted to
the Temple University Graduate Board

In Partial Fulfillment
of the Requirements for the Degree
MASTER OF SCIENCE

---

by
Nolan Conroy Barrette
December 2020

Thesis Approvals:

Dr. Atsuhiro Muto, Advisory Chair, Earth and Environmental Science
Dr. Nicholas Davatzes, Earth and Environmental Science
Dr. Ilya Buynevich, Earth and Environmental Science

ABSTRACT

Records of subglacial drainage features of previous ice sheets, such as tunnel channels (TCs), provide insight into drainage mechanisms of modern ice sheets. More than 60 tunnel channels were identified in the formerly glaciated landscape of Wisconsin, USA, in the footprint of the Green Bay Lobe of the Laurentide Ice Sheet. I used a combination of a reflection-seismic survey and a hydraulic-potential model to reveal the geometry of a TC and attempt to further understand the dynamics of TC formation. The seismic cross section along the Plainfield tunnel channel (PTC), 16 km up-ice from the terminal margin, shows an absence of a channelized feature in the subsurface. Therefore, the Plainfield tunnel channel likely initiates between 7-16 km up-ice from its terminus in a subglacial setting where the water-flow velocity may have increased, as dictated by the regional bed slope. Relatively fast subglacial water flow would have caused erosion at the ice-bed interface, whereas slower velocities produced little to no erosion of the underlying sediments. The hydraulic-potential model suggests a total area of ~107 km^2 for potential subglacial lakes up-ice from the PTC, although this estimate is not sufficient to account for the volume of water needed to form the channel. However, when water does pool in subglacial lakes, permafrost in the area helps to seal in large amounts of water at the ice-bed interface. Additionally, an increase in traction at the bed after a single discharge event likely facilitates supraglacial lake formation. The supraglacial water sources subsequently drain into the subglacial system, which can cause successive subglacial drainage events to occur. The results from the seismic cross-section and the hydraulic-potential model, along with inferences from previous studies, indicate that the

PTC is likely formed over several drainage events and had a substantial influence from moulin drainage of supraglacial water in addition to the water stored in subglacial lakes. The Laurentide Ice Sheet was able to store large amounts of subglacial water in this region due to the combination of an adverse bed slope, as well as expansive permafrost during the time of TC formation. This likely means that modern ice sheets, such as along the Western edge of the Greenland Ice Sheet or Thwaites Glacier in West Antarctica, could exhibit similar subglacial and supraglacial drainage behavior in areas with adverse bed slopes similar to this portion of the Laurentide Ice Sheet.

Dedicated to my parents - Paul and Tina,
my brothers - Jordan and Ethan,
and my grandfather - John,
for their constant love, support, and encouragement

ACKNOWLEDGMENTS

I would like to acknowledge the numerous individuals who helped me throughout my time at Temple University. First, I would like to thank my academic advisor, Dr. Atsuhiro Muto, for taking me on as a student and providing guidance throughout my thesis. I would also like to thank my committee members, Dr. Nicholas Davatzes and Dr. Ilya Buynevich, for their helpful input throughout the thesis process. I would like to thank the USGS Great Lakes Mapping Coalition for a portion of the funding that went into this project. I would like to recognize Dr. Lucas Zoet and Dr. J Elmo Rawling III for their help and expertise throughout the project and assistance with field work. I'd also like to thank Dr. Dante Fratta for letting me use his seismic equipment for this project. I would like to show my appreciation for Aaron Christensen, Analiese Genthe, and Alex Roccaro, who played a crucial role in the collection of data during field work. A special thank you to Shelah Cox, who always put a smile on my face and helped me navigate the formalities of graduate school. Finally, I would like to thank my colleagues for helping get me through these past couple of years: Justin Morris, Alex Roccaro, John Gallucci, Ashleigh Kirker, Tim Davis, Jesse Thornburg, James Berglund, Boyoung Song, Paul Choi, Louise Borthwick, Drew Spake, Chris Elofson, and all other previous and current graduate students that are a part of the memories of my time at Temple.

TABLE OF CONTENTS

Page

LIST OF FIGURES

CHAPTER 1

INTRODUCTION

Modern glaciers and ice sheets show varying patterns for subglacial drainage at the ice-bed interface (e.g., Andrews et al., 2014; Siegfried et al., 2016). Small changes in this drainage network can cause significant responses in glacier dynamics and flow speed (e.g., Flowers, 2015). For example, ice velocities during the summer melt season can be twice as high as during the winter because the increase in meltwater enhances bed lubrication (Bartholomew et al., 2010). Temporally-varying ice-stream elevations in Antarctica have been interpreted as the surface expression of subglacial-water drainage that can move km^3-scale volumes on relatively short time scales of months to years (Wingham et al. 2006; Fricker et al., 2007; Stearns et al., 2008). Often these large volumes of water move between subglacial lakes and can be observed directly in coastal regions as outburst floods (Goodwin, 1988). Observed outburst floods near Casey Station in East Antarctica have been associated with 1-2 m waterspouts from large crevasses within the Law Dome ice margin following an uplift of 4 m over a 20,000 m^2 area (Goodwin, 1988).

There are three broad categories of the subglacial drainage systems that affect ice dynamics (Figure 1): 1) an efficient channelized system interconnected with moulins and crevasses; 2) an interconnected, but unchannelized system that is influenced by the efficient system; and 3) an isolated passive system. The basal water pressure in these subglacial systems directly impacts ice velocity (Andrews et al., 2014). Conduits build pressure when meltwater inputs exceed the capacity of the conduits (e.g., Iken and Bindschadler 1986; Jansson, 1995). This acceleration is facilitated by the reduction in friction that occurs at the ice-bed interface when basal water pressure counteracts the ice overburden pressure (the pressure on the substrate from the weight of the ice) (e.g. Lliboutry, 1976; Fountain and Walder, 1998). An increase in basal water pressure reduces the effective pressure (the overall pressure at the bed) resulting in reduced ice-bed contact and subsequent decrease of traction at the bed (e.g., Bartholomaus et al., 2008).

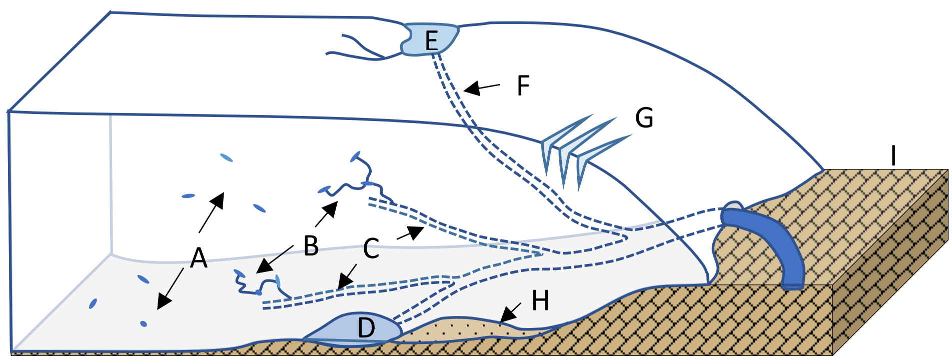

Figure 1. Glacier Schematic. Diagram of the terminus of a glacier highlighting aspects of the subglacial and englacial hydrologic systems. Letters represent the following areas: (A) isolated passive systems, (B) interconnected, unchannelized systems strongly affected by the efficient system, (C) efficient channelized system interconnected with moulins (F) and crevasses (G), (D) subglacial lakes, (E) supraglacial lakes, (F) moulins, (G) crevasses, (H) till, and (I) bedrock.

Borehole arrays drilled on alpine glaciers have been used to monitor the behavior of subglacial-drainage systems including subglacial-channel formation. Borehole measurements of water level and the electrical conductivity and turbidity of the borehole water have shown correlations between water-level fluctuations and subglacial drainage patterns dependent on the type of subglacial drainage network following rapidly rising meltwater (supraglacial, englacial, and subglacial sources) and precipitation inputs from the surface (Murray and Clarke, 1995; Gordon et al., 1998; Meierbachtol et al., 2013).

Boreholes connected to isolated fluid pockets typically show small diurnal variations in water level with similarly low values of turbidity and electrical conductivity, but water levels and amplitude of the fluctuation are largely independent between boreholes in the array. In contrast, boreholes connected to efficient channelized systems show identical water level fluctuations. Additionally, electrical conductivity and turbidity measurements show similar responses to fluctuations in water level, where an increase in water level generally shows increases in both electrical conductivity and turbidity. Neighboring boreholes that are inefficiently connected show temporal delays between water level changes with a dampened amplitude (Gordon et al., 1998). These observations show that inputs from supraglacial and englacial sources can initiate changes in subglacial networks and change the responses of subglacial-drainage systems due to source water. In addition, the alternating behaviors in the unconnected areas likely show transfer of mechanical support at the bed between connected and unconnected regimes following fluctuations of water pressure (Murray and Clarke, 1995; Gordon et al., 1998).

Borehole arrays can provide useful data characterizing the subglacial drainage systems, specifically their role in the fluctuation of fluid pressure critical to ice-flow velocity. However, these arrays are logistically intensive and difficult to employ on the larger scale necessary to study an entire lobe of a continental ice sheet (Andrews et al., 2014). Thus, they cannot be effectively used to study the flow and behavior of large ice sheets, which are both critical aspects of understanding ice sheet stability as the climate evolves and generates melt events. However, subglacial flow of fluid and sediment form distinct geomorphic features which can be preserved during glacial retreat. The structure and composition of these features can be used to infer the subglacial transport processes including the distribution, geometry, and attributes of isolated fluid volumes, connected but unchannelized fluid systems, and channelized fluid systems.

Along the Marine Isotope Stage 2 Green Bay Lobe (GBL) of the Laurentide Ice Sheet (LIS) in Waushara county, Wisconsin, evidence of subglacial-drainage systems exists, see Figure 2. More than sixty linear features have been identified and interpreted to be tunnel channels. The term “tunnel channel” is used for a channel formed from a subglacial river where the width of the river is equal to that of the channel with bank-to-bank flow (Clayton et al., 1999). Surface expressions of these TCs are typically ~0.15-0.5

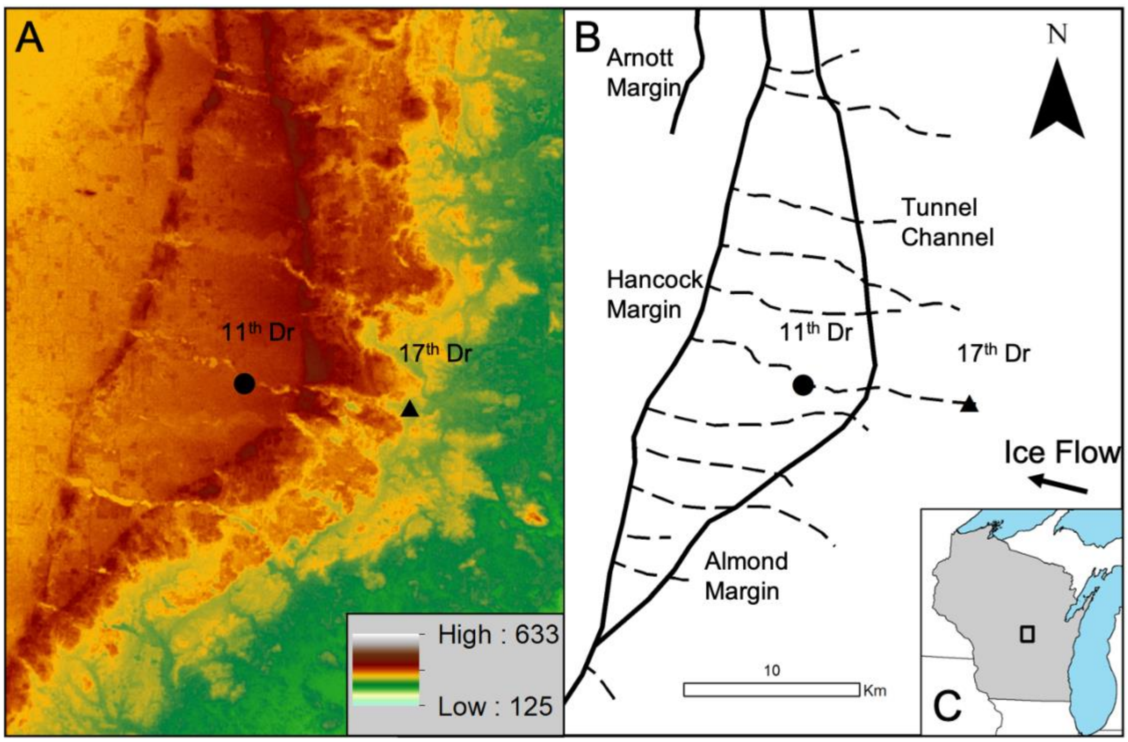

Figure 2. Field Locations. A) Shuttle Radar Topography Mapping (SRTM) elevation dataset underlain by a hillshade version of the dataset around the study region. The linear East-West trending features are interpreted as several TCs. These correspond to the surficial evidence of TC locations, shown in panel B as dashed lines. The solid lines in panel C show moraines of the region. The black circle denotes the Zoet et al. (2019) survey area, whereas the black triangle denotes my seismic survey site along the PTC. C) shows the state Wisconsin shaded in grey, with surrounding states in white and the Great Lakes in blue. The black rectangle shows the view extent in panels A and B.

km wide and ~5-30 m deep and extend up to ~15 km into the interior of the lobe. The TCs originate in the Green Bay lowland, to the east of the Almond moraine, and rise in elevation to the west where they breach the Last Glacial Maximum (LGM) terminal moraine. Sediment in outwash fans beyond the breached terminal moraine show distinct pits of boulders up to 2 m in diameter and span at least 150 m perpendicular to paleo-ice-flow direction (Cutler et al., 2002). Based on this, Cutler et al. (2002) interpreted the lithology as a high-discharge (~1000 m^3/s) outburst-flood deposit where boulders were rolled up the slope out of the Green Bay lowland and subsequently settled out west of the terminal moraine when water velocity decreased once the water was no longer confined by the channel. Similar features have been identified in other regions of the LIS (Livingstone and Clark, 2016) and similarly show a strong correlation to adverse bed slopes (Zoet et al., 2019). TCs show similar surface-morphologic features to tunnel valleys, such as those in Minnesota (e.g., Moores, 1989), but are interpreted to form differently. A tunnel valley is defined as a valley formed from lateral planation of a subglacial river where the river is significantly smaller than the width of the valley, similar to modern streams within flood plains (Clayton et al., 1999).

Surface expressions of TCs are not distinct channels, but rather surface depressions that formed by the collapsing of glacial sediments from the melting of buried ice after final retreat of the LIS. Current understanding of the TC formation is as follows (schematically shown in Figure 3): 1) subglacial channelized water erodes unconsolidated bed material resulting in a channel feature within the topography; 2) subglacial water no longer flows through the channel feature and ice occupies the area that was eroded by the channelized water flow; 3) the ice is buried by a combination of glacial and fluvial sediments while the GBL was retreating and advancing in the area. The ice persisted in the channel through several advancements due to permafrost acting as an insulator; 4) after the full retreat of the ice sheet regionally, permafrost and ice buried in the channel

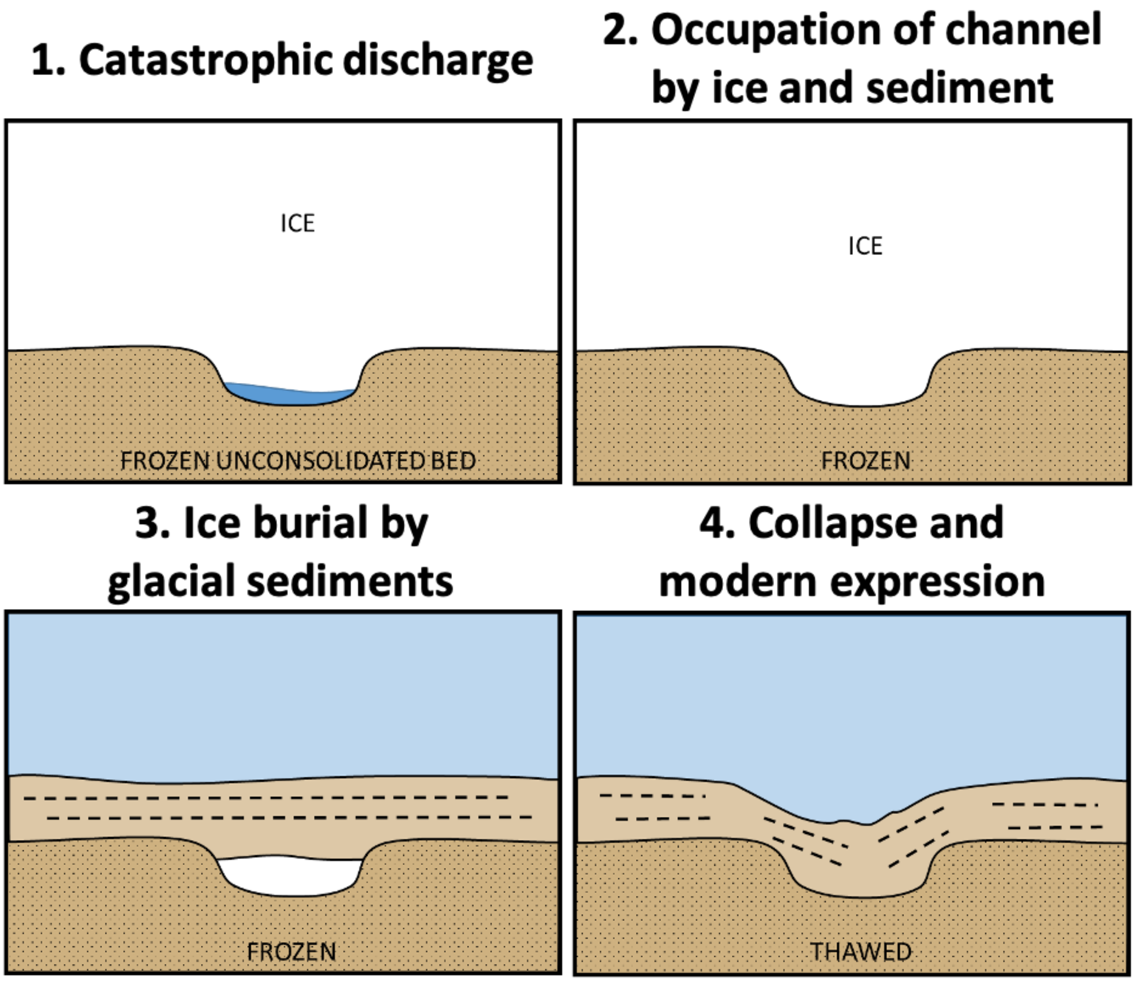

Figure 3. TC Formation. TC progression through time modified from Zoet et al. (2019). Time 1 shows a time in TC formation where water drainage erodes the unconsolidated bed. Time 2 shows ice filling the channel after water drainage occurs. Time 3 shows burial of ice in the channel by glacial and fluvial deposits during glacial retreat. Time 4 shows sediment collapse, represented by the dipping layers into the channel, and kettle lake formation, represented by the slumped surface topography, after the GBL had retreated from the area and the ice had melted.

melted, causing collapse of the overlying material and creating the surface expressions seen today (Zoet et al., 2019). The persistence of buried ice through several ice advances is not unique to the GBL and has been inferred through landscape features of other LIS lobes in north-central Wisconsin (Attig and Rawling, 2018). Kettle lakes are often present in TCs due to the collapse of overlying material after the melting of ice blocks followed by subsequent infiltration of water (Thwaites, 1943; Clayton et al., 1999).

The PTC, shown in panel A and B of Figure 2, is one of the largest TCs in the GBL area and has a surface expression that extends ~16 km into the interior of the lobe. The relative gradient along the TC shows one distinct change at the Almond recessional moraine (Figure 2**)** and corresponds to the apex of the regional topography. To the east, glacially upstream of this moraine, the topography shows an adverse bed slope, dipping in the upstream direction (towards the interior of the lobe), whereas west and downstream of the moraine, the topography dips towards the terminal moraine. The reflection seismic profile (Figure 4) revealed that the PTC cut through sedimentary layers with its own distinct internal layers draping the channel consistent with the collapse process described in Figure 3. The geometry of this channel segment, located ~7 km east of the terminal margin, is ~450-m wide, approximately equal to that of the surface expression, and 65-m deep, nearly 6 times deeper than the surface expression (Zoet et al., 2019).

Using the width and depth of the TC interpreted from reflection-seismic data, analysis of sediment core (grain-size distribution and sediment density) and estimated channel water velocity from studies of outwash-fan sediments, the sediment flux and duration of flow for TC formation can be estimated. Zoet et al. (2019) estimated the erosion rate using a modified version of the fluvial-sediment-transport model and deposition rate using a modified version of Stokes' settling law (Walder and Fowler, 1994). Zoet et al. 2019 determined the PTC required a minimum of 59 days to form from an average discharge of ~1000 m^3/s (Cutler et al., 2002). This would require a minimum

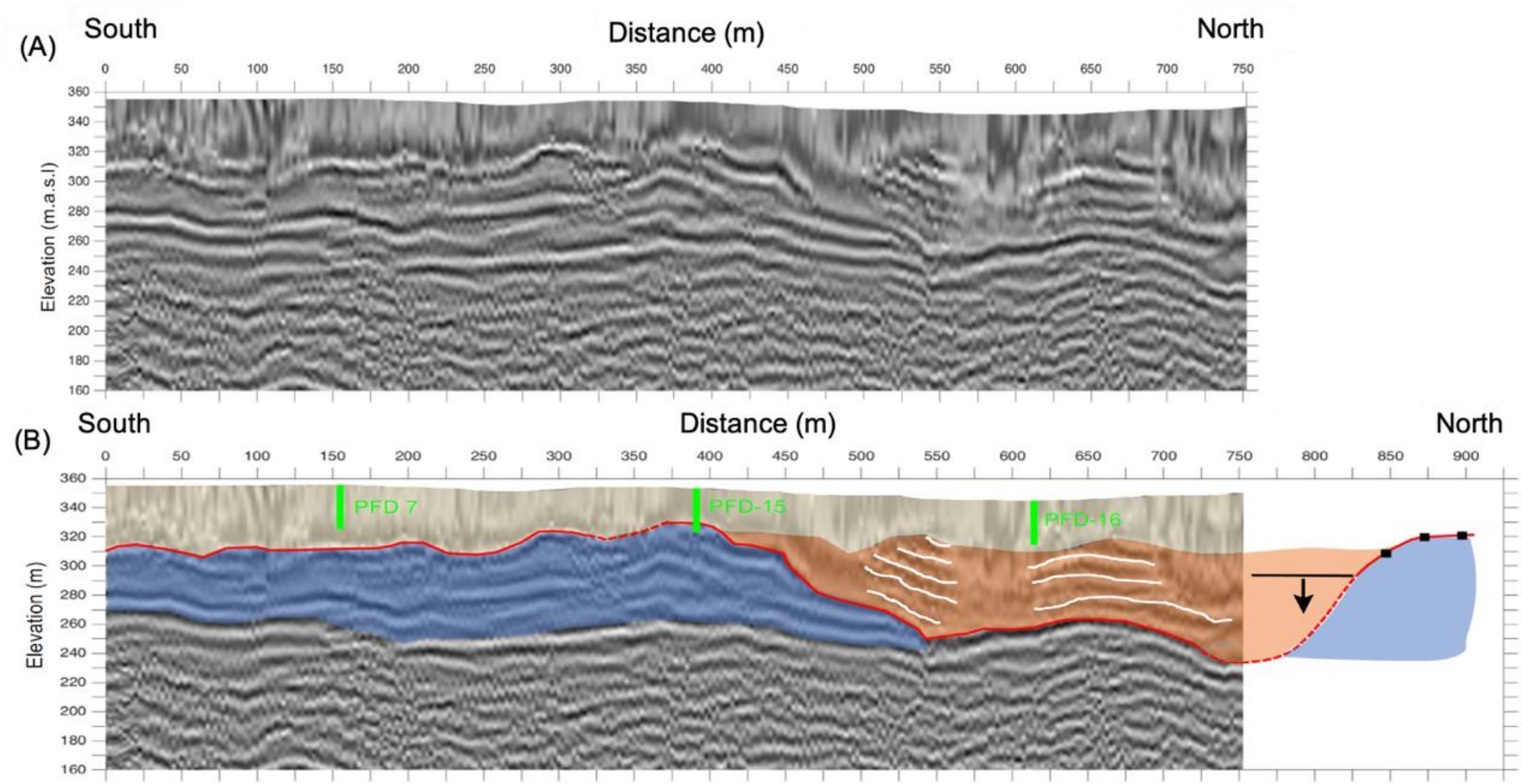

Figure 4. 11th Drive Cross-section. Reflection-seismic sections of the 11th Drive segment of the PTC from Zoet et al. 2019. Panel (A) shows the raw processed section and panel (B) is the interpreted active seismic section with depths included from the passive seismic survey, denoted with black squares on the right side of the panel. The red line is the inferred subglacial surface after TC formation had eroded ~65 m into preexisting subglacial sediments (blue region). The orange region shows collapsed material following the melting of buried ice. Horizontal white lines in this region indicate dipping layers similar to those hypothesized in Figure 3. Ranges of seismic velocities are shown in white with the black showing a lower-velocity weathered layer ~30 m deep.

water volume of 5 km^3 over a maximum area of 30 by 12 km based on the map of the hydraulic potential, meaning the average lake depth for one continuous lake would be ~14 m (Zoet et al., 2019). They determined such a large subglacial lake would not form only ~15 km from the terminal moraine based on the reconstructed ice thickness of the GBL (Colgan, 1999), and thus, it was unlikely the water was sourced solely from one subglacial lake. Consequently, they suggested two scenarios of TC formation: 1) the TC formed from multiple drainage events from smaller subglacial lakes; or 2) the water originated from a combination of subglacial and supraglacial sources that penetrated to the bed.

It is not yet clear which one of the two scenarios suggested by Zoet et al. (2019) formed the PTC, but they determined that both would cause a decrease in porewater pressure in till proximal to the channel, resulting in strengthening of the till and additional resistive force from the bed against the ice flow. A single drainage event would cause till strengthening in an 840-m zone on either side of the channel, whereas multiple 15-day drainage events would cause a 240 m zone on either side and provide ~5 times less resistive force during each event (Zoet et al., 2019). Increased basal normal traction corresponds to increased frictional resistance and thus locally reduced ice velocity. Reductions in ice velocity have been observed after large drainage events in modern glaciers in Alaska (Bartholomaus et al., 2008) and Greenland (Sundal et al. 2011). Estimated shear stress at the base of the GBL during LGM of 7-25 kPa (Colgan, 1999) indicates that till strength in the vicinity of the TC could have increased by a factor of 7-25 for a 15-day drainage event and led to a local thickening of ice by ~15 m (Zoet et al., 2019). A local reduction in flow velocity above the zone of increased frictional resistance would cause a local ice thickening and create potentially large supraglacial lake basins to form up-ice (Zoet et al., 2019). This could explain the supraglacial source of additional water and why alternative drainage routes could have been followed in subsequent formations of other TCs (Zoet et al., 2019).

Hypotheses of Zoet et al. (2019) rely on knowing the overall morphology of the PTC. However, data showing where the channel initiates and whether the channel changes its morphology along its path is lacking. This research addresses this gap by providing additional active-source seismic data to constrain the channel geometry as well as by updating the calculation of the regional hydraulic potential. Together, these constraints address the plausibility of the competing TC formation scenarios.

CHAPTER 2

RESEARCH OBJECTIVES AND HYPOTHESES

2.1 Background and Implications

Glacial hydrologic dynamics at the ice-bed interface depend on varying subglacial drainage patterns which modulate fluid pressure. Studying paraglacial landforms, such as TCs, allows us to infer subglacial processes at the ice-bed interface. TC geometry allows for the estimation of erosion and deposition rates, which dictate the duration of formation and the water volume. The seismic cross-section of 11th Drive (Figure 4) analyzed by Zoet et al. (2019) only shows the morphology of the PTC in one location. Additional cross-sectional geometries along the TC can be used to characterize subglacial-drainage behavior in this region. Constraining the varying geometry and spatial extent of the TC is necessary to differentiate between possible explanations for TC formation as well as water-source locations that exist both subglacially and supraglacially within the GBL (Zoet et al., 2019). The combination of water-source locations and TC formation processes will help elucidate the subglacial processes controlling the glacial dynamics of the GBL. How subglacial and supraglacial water within the GBL was organized and behaved gives us insight into glacial dynamics that cannot be extensively observed in modern glaciers. The resulting characterization can thus be used to better model the observed and future behavior of modern ice sheets including their response to changes in meltwater inputs accompanying climate change.

2.2 Research Objectives

The goal of this research is to determine the spatial extent and variability in cross-sectional area of the PTC by uncovering the geometry of the PTC up-ice from a transect previously surveyed by Zoet et al. (2019). Unveiling the geometry at this new location will indicate: 1) if the PTC extends in the up-ice direction beyond the Almond moraine, and 2) how the change in geometry of the PTC records the potential flux of water in the channel. I will test the following two hypotheses in order to achieve these objectives.

2.3 Hypotheses

1. The cross-sectional area of the PTC is smaller upstream from the previously surveyed location.
2. The Plainfield tunnel channel formed over multiple drainage events with a significant volume of water coming from supraglacial sources.

I base my first hypothesis on the following lines of evidence: 1) The topography shows a large, adverse bed slope in relation to regional ice-surface slope and 2) the surface expression of the PTC becomes more faint and less discernable further up-ice and into the Green Bay lowland. The first line of evidence, that the regional topography exhibits an adverse bed slope in this region, can be seen in Panels A and B of Figure 2. The surface dips steeply to the east and up-ice from the Almond margin. When the ice was present in this region, the topography would have been isostatically depressed (e.g., Anderson and Anderson, 2010). Ice is usually thicker in the interior of ice sheets in the accumulation area (e.g., Hooke, 2005), and therefore would steepen the adverse bed slope in the region east of the Almond margin due to the greater mass of ice over the bed topography. The presence of an adverse bed slope in this region is significant due to the affect that sufficiently steep adverse bed slopes can have on subglacial water flow. Ice surface slope generally dictates the subglacial water flow, as it is ~11 more important compared to the slope of the bed topography. However, steep adverse bed slopes can begin having a greater effect on subglacial water flow when they approach an order of magnitude greater than the surface slope (Shackleton et al., 2018; Zoet et al., 2019). This relationship is derived from the hydraulic potential calculation from Shreve (1972), where the hydraulic-potential gradient is proportional to the ice surface slope multiplied by the density of the ice, while also being proportional to the bed surface slope multiplied by the difference in density between the ice and water. Because ice is roughly ninety percent the density of water, the bed slope only affects subglacial water flow at the same magnitude as the surface slope when the bed slope is an order of magnitude greater. (Zoet et al., 2019).

The second line of evidence supporting hypothesis 1 is that the surface expression of the PTC becomes less discernable up-ice and to the east of the Almond moraine. Figure 5 shows the current surface topography near the 11th Drive segment from Zoet et al. (2019) and near 17th Drive, ~9.5 km up ice from the 11th Drive segment. Most notably, the 11th Drive segment has a distinct depression on the surface. On the other hand, 17th Drive shows an uneven, hummocky topography without a clear depression.

My second hypothesis is based on the results of a previous study by Zoet et al. (2019) that: 1) the total area of potential subglacial lakes is only a fraction of that needed to form the PTC; and 2) the local ice thickening that occurs after a drainage event allows one or several potentially large supraglacial lakes to form. The maximum potential

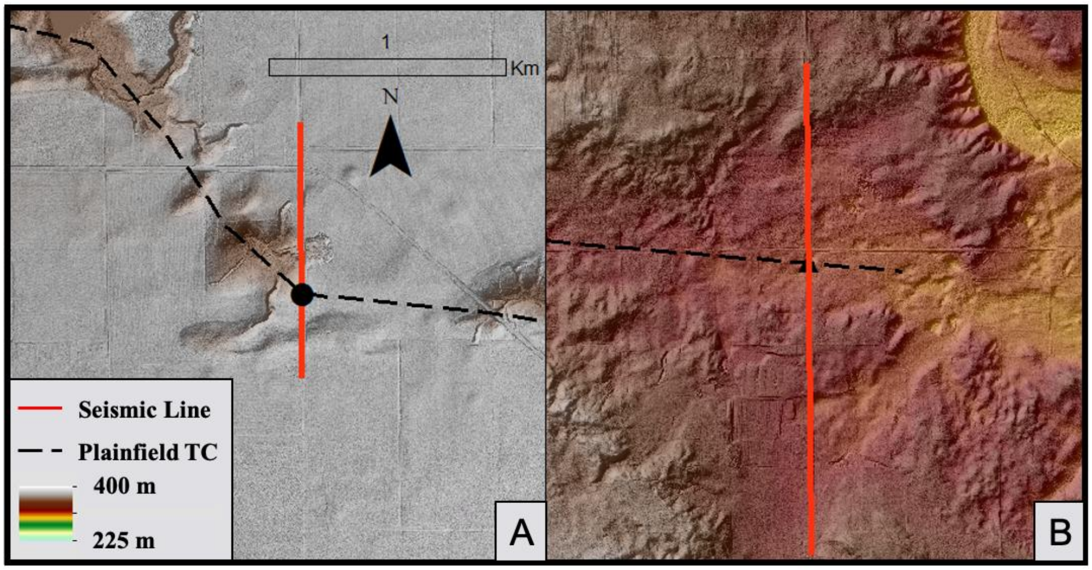

Figure 5. TC Surface Expression. Modern topography along the PTC. Panel (A) shows the portion around 11th Drive, whereas panel (B) shows the portion around 17th Drive. The vertical lines on both panels show the approximate length of each seismic line.

subglacial lake area calculated by Zoet et al. (2019) is limited to 360 km^2. Given this area, Zoet et al. (2019) calculated that the depth for one contiguous subglacial lake would be ~14 m, which is within the range of observed subglacial lake depths underneath the AIS (Siegert, 2000). However, they argue a subglacial lake this large is unlikely to form so close to the terminus of the ice sheet. For this reason, they conclude it is more likely that the formation of the TC occurs over multiple, smaller drainage events.

Zoet et al. (2019) also showed that once a subglacial-drainage event initiates, traction at the ice-bed interface increases due to the till strengthening because drainage of the porewater in the surrounding till through the channel reduces porewater fluid pressure. The corresponding reduction in ice sheet velocity above this strong region would then result in the local ice thickening (Zoet et al., 2019). This would in turn allow supraglacial lakes to form in the region behind the thickened ice that could initiate or contribute to future subglacial water outburst events by draining from the ice surface to the bed through moulins. Supraglacial lakes in Greenland have been shown to lose large amounts of water in a given melt season and can account for volumes greater than 0.5 km^3 across a total area of 6500 km^2 (Fitzpatrick et al., 2014). This is a significant volume compared to the 5 km^3 estimated to form the PTC, assuming most of the water contributing to the formation of the PTC is subglacial in origin. Additionally, my study area is substantially smaller than that of Fitzpatrick et al. (2014) and likely would not have the same volume of supraglacial water.

To address these hypotheses, I conducted a reflection-seismic survey at a transect across the PTC up-stream from the transect previously surveyed by Zoet et al. (2019). I also created a subglacial hydraulic-potential model to identify potential subglacial lakes. The reflection-seismic data addresses the first hypothesis regarding the change in cross-sectional area of the PTC as the channel progresses up-ice from the terminal moraine. The subglacial hydraulic-potential model will address the second hypothesis regarding the hypothesized multiple drainage events to form the PTC by providing estimates of area of the subglacial lakes underneath a section of the GBL. This estimate, in combination with the change in cross-sectional area of the PTC, will provide an insight into the subglacial hydrology near ice-sheet margins.

CHAPTER 3

METHODS

For this study, I used active-source seismic reflection to image the expression of the PTC buried in the subsurface. I conducted one survey line along a local roadway, which is perpendicular to the PTC, and obtained a true-width profile of the subsurface features. I then determined potential areas of subglacial lakes by calculating the second derivative of the subglacial hydraulic potential for a ~70 km by ~120 km section of the GBL surrounding the PTC to quantify the area of potential subglacial lakes underneath the ice sheet in this region. I based the subglacial hydraulic potential calculation on a modeled ice surface and the modern topography derived from Shuttle Radar Topography Mission (SRTM) bed elevation data, which was isostatically adjusted based on ice thicknesses from the modeled ice surface to account for the isostatic rebound that has occurred in the region since LGM.

3.1 Reflection-Seismic Survey

I collected reflection-seismic data using the Geometrics StrataVisor NZ^{TM} seismograph with 48 of the 24-Hz vertical-spike geophones at 6 m spacings. The StrataVisor can only record 24 channels at once, so two sets of 24-channel recordings were acquired at each source location. For the seismic source, I used a GISCO EES-Mini 208 Joule accelerated weight drop mounted on the back of a vehicle. This type of source (Figure 6) uses a heavy piston that is dropped on to the surface of the earth to create energy that radiates through the subsurface. A strike plate is used along with a trigger mechanism that senses when the source hits the plate. The trigger mechanism then relays to the recorder that data acquisition has started. The piston is reinforced by resistance bands to add additional energy to each shot, which helps produce data with a higher signal to noise ratio. The source was triggered between 12 m and 144 m off the end of the geophone array at 12 m intervals for a total of 12 shot locations for one spread of 48 channels. Figure 7 shows a schematic diagram of this survey geometry. The

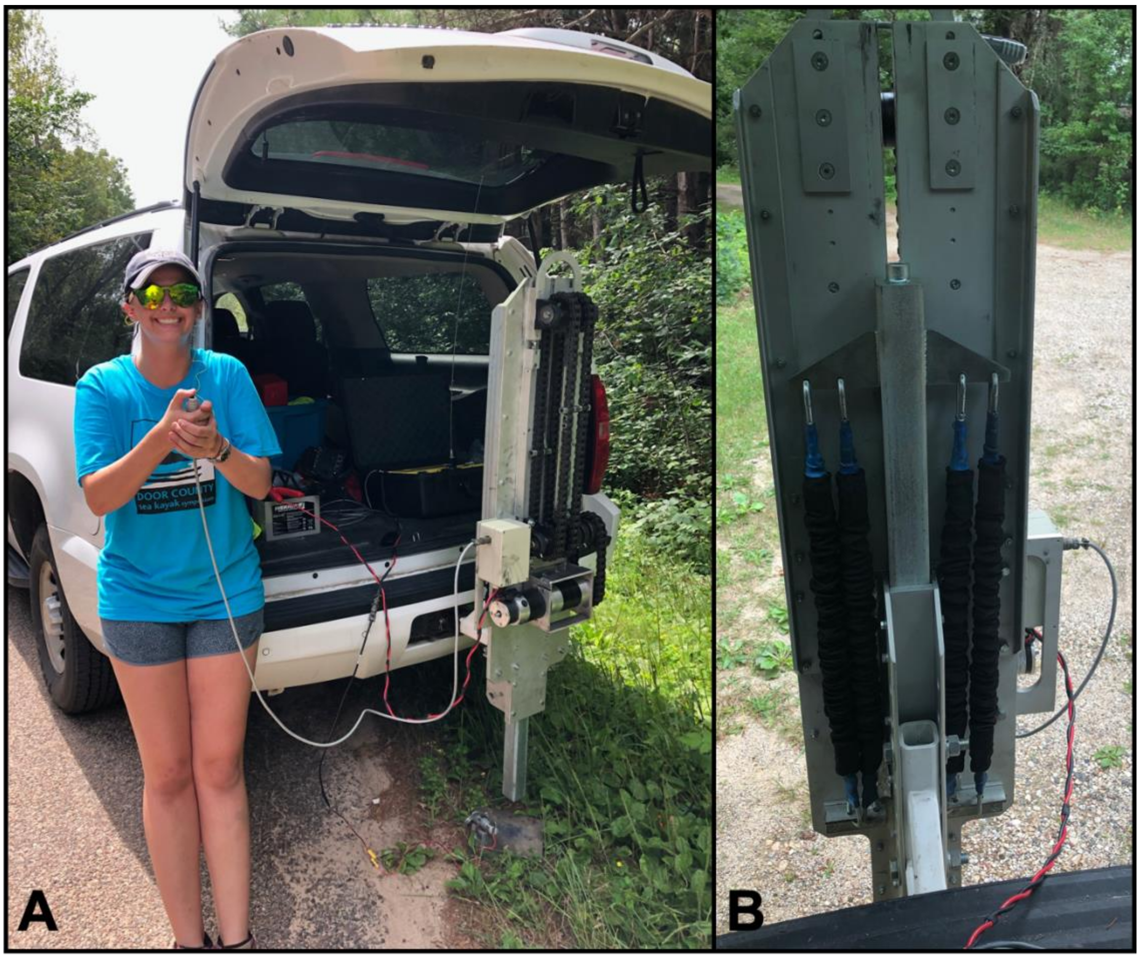

Figure 6. Seismic Source. Images of the seismic source, GISCO EES-Mini 208 Joule accelerated weight drop, attached to the hitch of the field work vehicle. A) View of the seismic source with the strike plate in position underneath. Field assistant Analiese Genthe is preparing to start data acquisition. B) View of the 'hammer' of the accelerated weight drop. The piston is located in the center of the apparatus, with 2 resistance bands on either side to add additional force when triggering the source.

geophone array was manually moved to a new spread location by leapfrogging the first half of the array past the second. The 17th Drive survey required 7 days of data collection and totaled 2,736 m in length. This survey set up results in nominally 12-fold *P*-wave seismic reflection data with the common-depth-point (CDP) spacing of 3 m and shot-receiver offsets between 12 and 426 m. To minimize environmental noise, data acquisition was halted when the wind was strong and vehicles, such as trucks, tractors, and lawnmowers, were passing nearby. Even with this effort, residual noise is expected. To enhance the signal-to-noise ratio (SNR), four shot recordings were stacked together and saved as one single recording.

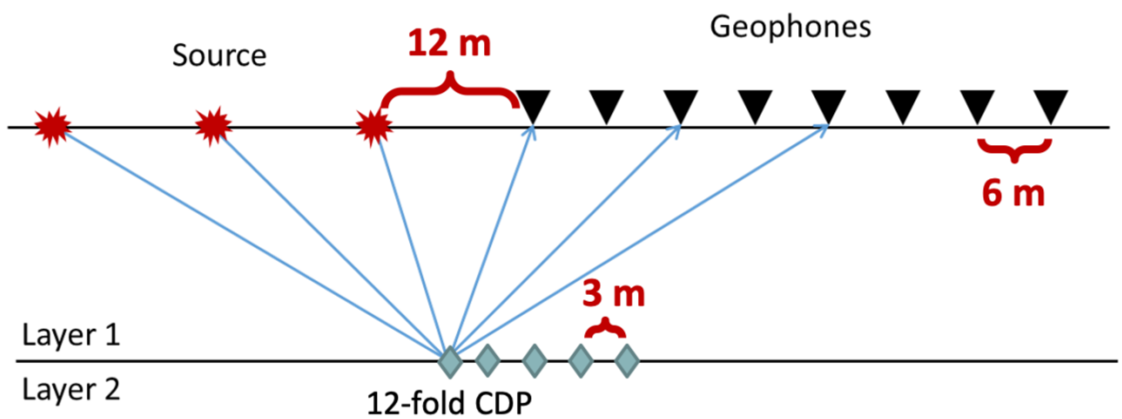

Figure 7. CDP Schematic. Schematic diagram of the shot-receiver locations during a reflection seismic survey. Source locations are shown in red, geophones are shown as black triangles, and the CDP locations in the subsurface are shown with teal diamonds.

I processed the data following standard shallow two-dimensional land-seismic techniques (e.g., Pugin et al. 1996; Baker, 1999; Pugin et al., 2009; Thomason et al., 2018) using a combination of Seismic Unix™, Globe Claritas™, and MATLAB® software. This workflow is shown in Figure 8. Raw data from the recorder was converted from SEG-2 to SEG-Y format and merged to form one 48-channel recording for each shot location. I added geometry information (locations of shots and geophones along the transect) to the dataset and examined the preprocessed data to ensure the shot-receiver locations are correct for each record. The geometric information keeps track of the distance relationship between the shot location and each receiver location, allowing for accurate velocity estimates in the subsurface at a later step. Single traces within a shot gather from specific noisy geophones were canceled out, or killed, prior to any further analysis. Similarly, the ground roll (coherent seismic energy that travels along the ground surface) was muted so CDP gathers are not compromised by the ground roll and reflections can be seen during the velocity analysis (Pugin et al. 1996; Baker, 1999; Pugin

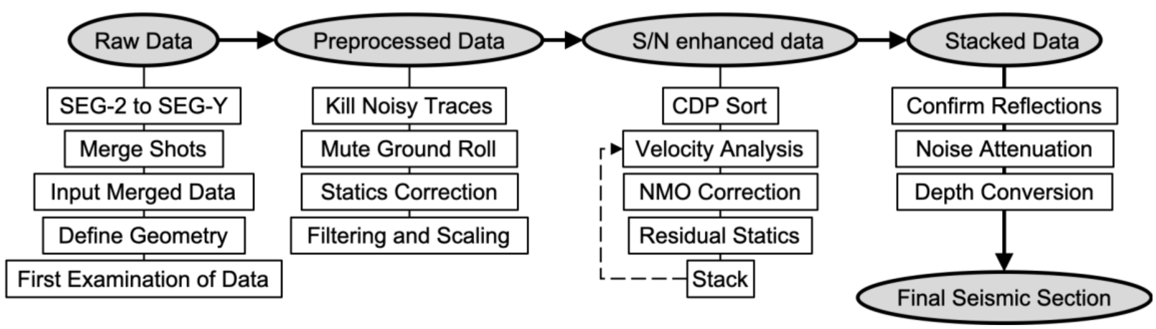

Figure 8. Seismic Workflow**.** Processing workflow for processing the 17th Drive shallow active seismic reflection data**.**

et al., 2009; Thomason et al., 2018). A sample shot gather with muted ground roll and killed noisy traces is shown in Figure 9. Static corrections were applied to correct for the near-surface, low-velocity weathered layer based on refracted arrivals manually picked from each shot gather. The velocity model for this low-velocity weathered layer is shown in Figure 10. Then, deconvolution and bandpass filters were applied to strengthen the SNR. Shot-consistent deconvolution was applied using a window length of 100 ms and a gap length of 10 ms. The bandpass filter passed the band of 60 – 150 Hz, with a 20-Hz low-frequency roll off and a 30-Hz high-frequency roll off. Next, the enhanced SNR data are sorted into the common depth point (CDP) to combine traces across multiple shot gathers that correspond to the same subsurface CDP location. I then performed a velocity analysis on the CDP-sorted data, where an initial stack is made based on a first rough estimate of a velocity profile. A constant-velocity window is used during this analysis, where each CDP trace is adjusted based on a single velocity for the entire trace length. When a velocity is appropriate for a given area, a sharp reflector will come into focus at a given two-way time across multiple traces that constitute a single CDP trace. This constant velocity analysis is used across all 869 CDPs for this survey. After the velocity analysis, a normal-moveout (NMO) correction is applied that executes a shift to all CDP traces across the survey domain by the corresponding velocity values. Additionally, I apply residual-statics corrections, which optimize stack power along a CDP trace by slightly adjusting the arrival time of individual raw traces that make up a CDP trace. I performed the sequence of velocity analysis, NMO correction, and residual statics correction four times until the stacked section was showing clear reflectors. A final stacked seismic section was then produced based on the final velocity profile. The final stacked section was then corrected for ground topography and converted from the time domain to absolute elevation using the aforementioned NMO velocity model.

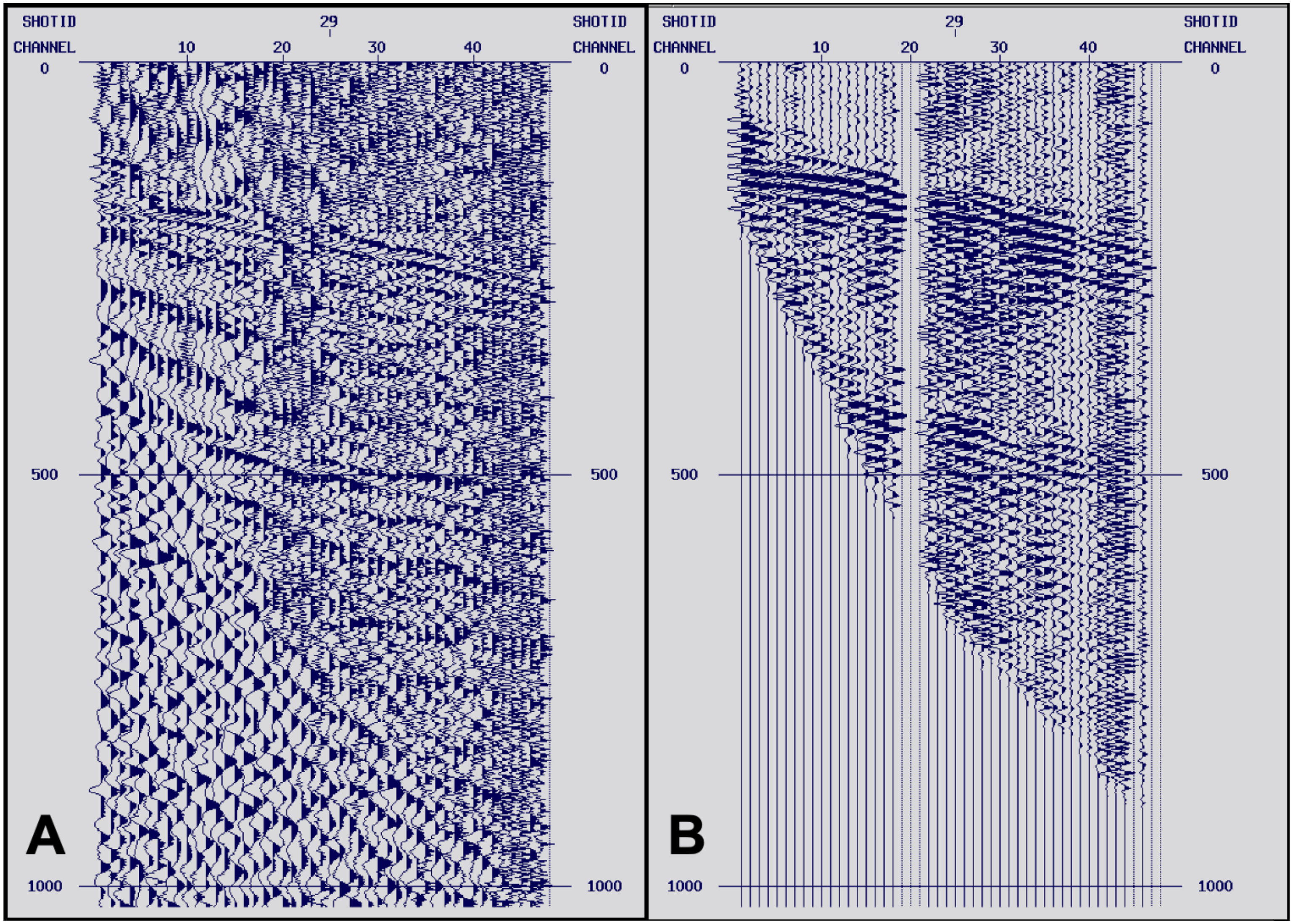

Figure 9. Example Shot Gather. Example of a shot gather as a raw dataset and pre-processed dataset. A) Raw dataset with a 75 ms AGC window applied. B) Pre-processed dataset with killed noisy traces, ground roll muting, and a bandpass filter of 40-60-150-180 Hz.

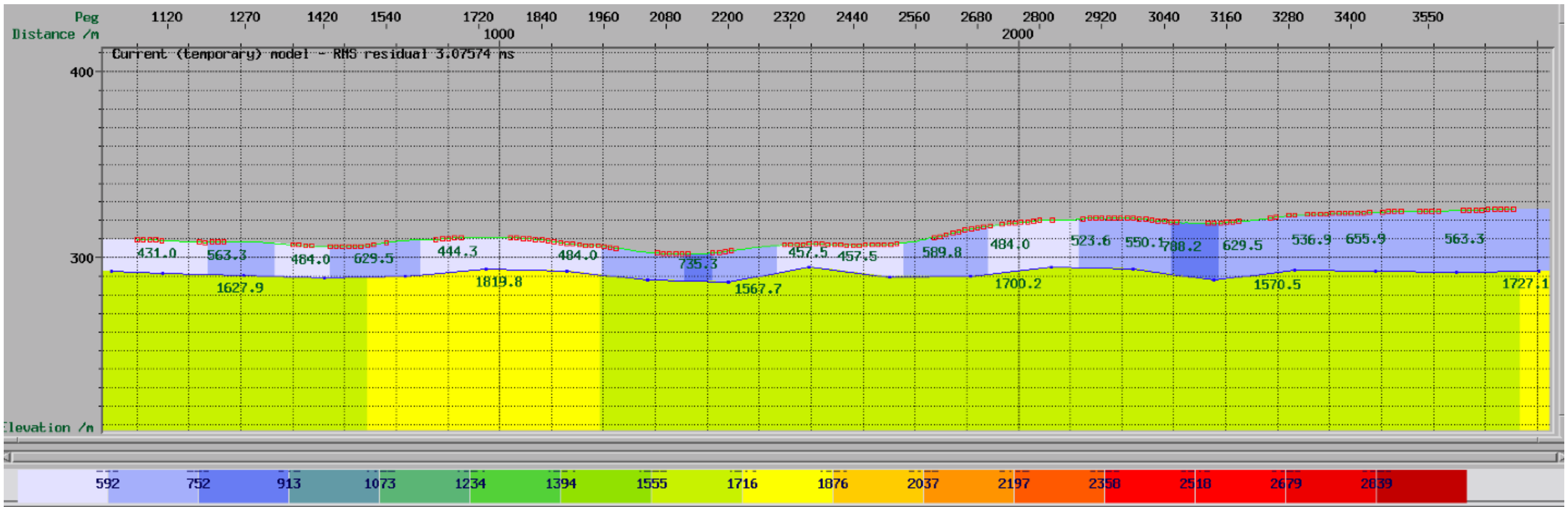

Figure 10. Weathered Layer Model. Shallow, upper layer velocity model across the 17th Drive seismic velocity survey based on refracted arrival times.

3.2 Subglacial Hydraulic-potential Model

Derivatives of the hydraulic-potential indicate areas where subglacial lakes can form. This method of locating potential subglacial lakes has been used previously across paleo-ice sheets such as the LIS (Zoet et al., 2019) and the Fenno-Scandian Ice Sheet (Shackleton et al., 2018). Zoet et al. (2019) used the first derivative calculation, which indicates regions where water flow is slow and subglacial lakes could have formed. My calculation used the second derivative, which is a better indicator of potential subglacial lakes (Sergienko, 2013). This concept can be seen in Supplementary Figure A1, where an idealized topography is used and the divergence of the topographic gradient is calculated. The divergence of the hydraulic-potential gradient can be approximated similarly, where positive values correspond to sinks in the dataset, or where subglacial lakes would form. Additionally, Zoet et al. (2019) based the hydraulic-potential model on a series of one-dimensional profiles stacked to form a 2D matrix of the hydraulic potential. I update this model by calculating the second derivative of the hydraulic-potential with a two-dimensional approach, instead of a simple one-dimensional profile approach. I located the potential subglacial lakes by first obtaining the hydraulic potential across the study area, then taking its derivative twice.

The hydraulic potential ϕ was calculated following the method of Shreve (1972):

$$\phi = \rho_w g Z_b + \rho_i g (Z_s - Z_b) \tag{1}$$

where ρ_w is the density of water, ρ_i is the density of ice, g is the gravitational acceleration, Z_b is the elevation of the bed, and Z_s is the elevation of the ice surface. Prior to the calculation, I adjusted the bed elevation based on isostatic equilibrium to account for the isostatic rebound to the modern topography since the LGM. I calculated the hydraulic potential at each discrete grid cell (the base topography data and grid-cell size are explained below). The gradient at each grid cell was then calculated based on the surrounding 8 cells, resulting in the subglacial hydraulic-potential gradient, which was subsequently differentiated to obtain the divergence of the hydraulic-potential gradient (second derivative of the hydraulic potential).

The two main inputs for these calculations are the current surface elevation and the ice-surface elevation estimated at the LGM. I obtained the current surface elevation from the 1 arc second digital elevation model (DEM) from the Shuttle Radar Topography Mission (SRTM). At the latitude of the study area (~45° N), the grid spacing of the SRTM DEM was ~27 m. Twelve SRTM tiles were mosaicked together using Esri ArcMap software, spanning 42° – 45° N and 88° – 90°W, using the Mosaic to New Raster tool with default settings and an output spatial reference set to UTM Zone 16 N. This extent was then reduced to focus around the PTC based on the bedrock map of the area provided by the Wisconsin Geologic and Natural History Survey (WGNHS) (J. Elmo Rawing III, personal communication, 2020), resulting in an area of ~111 km by ~118 km (Figure 11).

At this point, the surface topography needs to be adjusted due to the Almond recessional moraine (Figure 2) not being present at the time of the TC formation; the ice margin was at the extent of the terminal moraine - the Hancock margin. Current surface elevation was smoothed using a local regression filter with the weighted linear least squares and a second-degree polynomial tool built within MATLAB. This specific filter assigns lower weight to outliers in the regression and assigns a zero weight to data outside six mean absolute deviations. The filter was applied first to each row of the elevation dataset, followed by each column of the elevation dataset. In both filtering steps, the filter was applied with a span of five percent of the total data points within each respective row or column. This was found to best approximate the regional topography and not over-smooth the topography, which would remove important topographic variations that control the hydraulic potential.

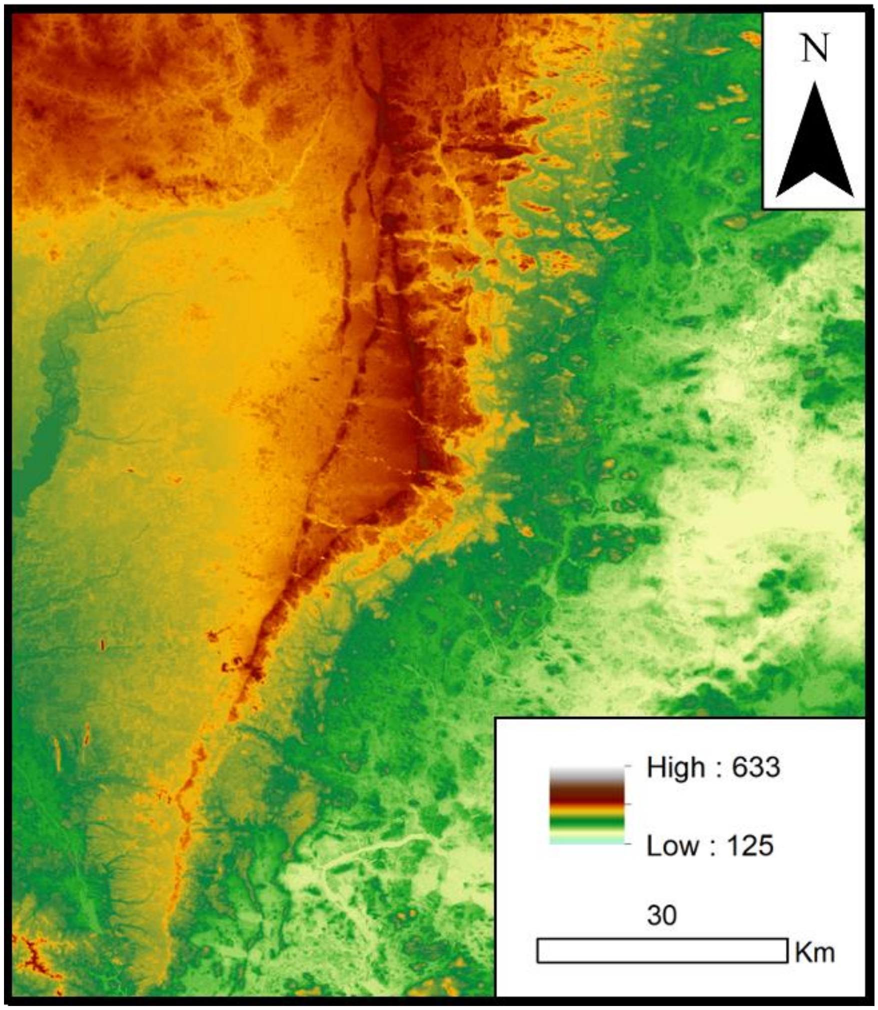

Figure 11. Hydraulic Potential Model Area. SRTM elevation in the hydraulic potential model domain showing the modern topography used within the model calculations prior to isostatic adjustment.

I derived the ice surface from the ice-surface topography of the 15-18 ky Green Bay Lobe, the Johnstown-Hancock phase of the MIS2 ice advance, reconstructed by Clark (1992). I digitized and georeferenced this ice-surface topography using ArcMap and created a shapefile containing equal ice-surface elevation profiles (Figure 12). This shapefile was brought into MATLAB and combined with the moraine-elevation points from the WGNHS terminal-moraine map (J. Elmo Rawing III, personal communication,

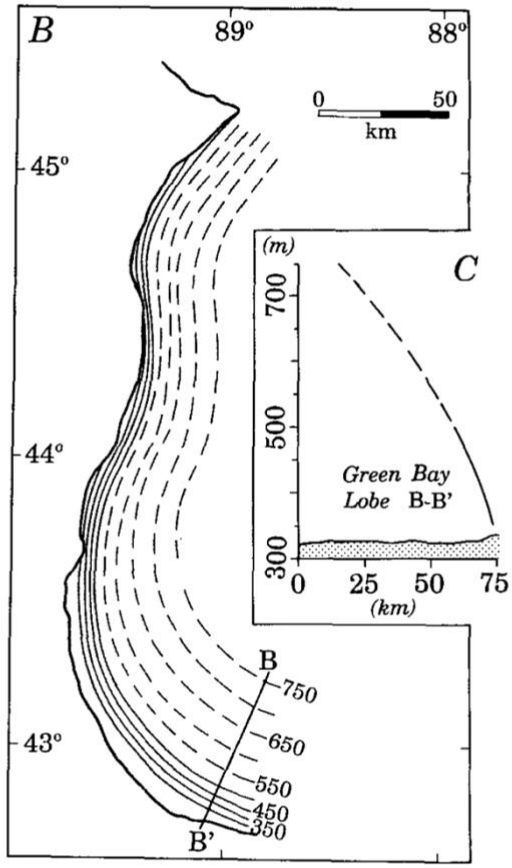

Figure 12. Ice Surface Reconstruction. Reconstructed ice-surface morphology of the MIS-2 (15-18 ka) Green Bay Lobe, from Figure 9B and 9C of Clark (1992). Contour lines in B are at 50 m intervals. C shows a typical longitudinal ice-surface profile for the MIS-2 Green Bay Lobe.

2020). This method uses the ice-surface reconstruction from Clark (1992) and assumes that the ice intersects the bed topography at the apex of the modern-day moraine. The following five model fits were investigated to best approximate the ice surface and its intersection with the bed topography: linear interpolation, nearest neighbor interpolation, cubic spline interpolation, thin-plate spline interpolation, biharmonic interpolation, and local quadratic regression. Figure 13 shows the chosen model surface fit, whereas the other models can be found in Appendix A, Supplementary Figures A2-A6, for a visual comparison. The linear, nearest neighbor, and cubic spline interpolation

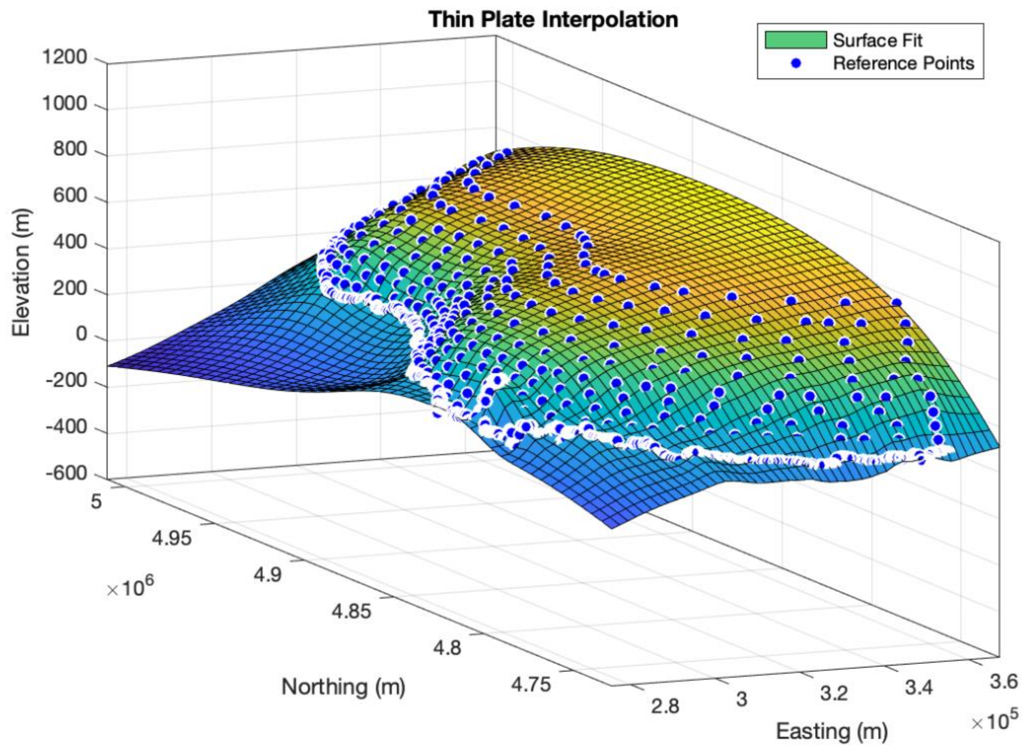

Figure 13. Ice Surface Model Fit. Thin-plate spline interpolation method ice-surface fit. Reference points correspond to the equal-elevation lines from Clark 1992. Viewpoint is looking Northeast in the up-ice direction.

methods were all ruled out upon first inspection due to the constant elevation of the surface fit that corresponds to the up-ice and central portion of the GBL, see Supplementary Figures A3, A4, and A6. This is unrealistic based on previous ice-surface reconstructions of the GBL (Clark 1992; Colgan 1999). The remaining three models show similar fits close to the reference points for each method. However, the biharmonic interpolation and local quadratic regression show significant, erroneous modeled values at distances far from the reference points used to fit the surface. It is important to note that most of the locations described as erroneous were outside of the footprint of the GBL and were ignored by the model. However, this error was accentuated within the footprint when comparing these three models in the up-ice and central portion of the GBL. This location was similar across the biharmonic interpolation and local quadratic regression methods in that a relatively steep gradient exists as the modeled surface approaches the edge of the model domain. In contrast, the thin-plate spline interpolation method shows a shallower gradient as the surface approaches the model domain. This relatively shallower gradient is consistent with studies from both Clark (1992) and Colgan (1999) which find that away from the terminal margin, ice surface slopes are generally shallower and more consistent than those near the margin.

The divergence of the hydraulic-potential gradient (second derivative of the hydraulic potential) represents how the gradient of the hydraulic potential is changing. Highly positive divergence corresponds to ‘sink’ locations where general flow paths are directed to, whereas highly negative divergence corresponds to ‘source’ locations where flow paths are directed away from. I produce a map of potential subglacial lake locations based on where the divergence is positive. I then clipped the dataset to only show the top ~98% of the positive values based on the likelihood that all locations of potential subglacial lakes do not fill at the same time. It is more likely that a subset of subglacial lakes fill and subsequently drain into other subglacial lakes downstream, similar to subglacial lake drainage observed beneath Thwaites Glacier (Smith et al., 2017) or lower Mercer and Whillans Ice Streams (Fricker and Scambos, 2009). In ArcMap’s Raster Calculator tool, I used the Map Algebra expression “’Raster’ > 0.3” to return a raster dataset where a value of 1 represents the divergence of the hydraulic potential gradient above the threshold mentioned above. Then, the raster values equal to 1 are extracted using the Extract by Attribute tool and converted to a polygon shapefile using the Raster to Polygon tool. Conversion to a polygon dataset allowed for independent potential subglacial lake areas to be identified. Additionally, I performed a calculation of the geometry to estimate the area within each polygon in the dataset. Prior to geometry calculation, an additional field was added to the shapefile and assigned a float variable type with precision and scale both set to six. This gave the calculation a precision to the nearest 10 m^2. After the geometry calculation, I filtered the dataset using the Select tool to only show polygon features greater than 0.25 km^2 based on the square of the minimum length of identified subglacial lakes in Antarctica (Popov and Masolov, 2007; Wright and Siegert, 2012). This assumes that the LIS and AIS have similar subglacial behaviors, which is likely an appropriate first-order approximation based on comparable percentages of the terminal-margin draining via ice streams (Margold et al., 2015). Additionally, the polygons within 2-3 km of the terminal moraine were removed based on reconstructed ice-surface slope of Colgan (1999) for the Johnstown-Hancock (MIS-2) phase of the LIS. This reconstruction shows a steep ice slope as the ice sheet approaches the terminus, where water likely would not pool due to the surface slope being ~11 times more important in the movement of subglacial water compared to the topographic slope, discussed previously in Chapter 2 (Shackleton et al., 2018; Zoet et al., 2019).

CHAPTER 4

RESULTS

4.1 Reflection-Seismic Survey

Figure 14 shows the final stacked cross-section from the reflection-seismic survey. The figure shows a cross section of the final depth-converted data along with a cross-section with interpretations overlain. The seismic data shows two distinct reflectors. The shallower reflector is bright, indicating a large p-wave velocity contrast, and spans approximately 500 m between ~900 m and ~1400 m along the cross section transect at an elevation that varies between ~230 m and ~250 m above sea level, whereas the deeper reflector spans the entire cross section at an elevation that varies between ~200 m and ~230 m above sea level. I estimated the velocity of the shallower reflector to be between 1550 m/s and 1600 m/s, whereas the deeper reflector is between 1600 m/s and 1800 m/s.

I utilized a measured stratigraphic sequence in the area (J. Elmo Rawling III, personal communication, 2020), along with the subsurface weathering model (Figure 10) to aid in my interpretation of the seismic cross-section. Sediment stratigraphy in the 17th Drive location is inferred from a deep sediment bore recovered at the 11th Drive transect (Zoet et al., 2019). This ~125 m boring, specific samples shown in Figure 15, shows that the lithology changes from a distinctly sandy sediment near the surface, to interbeds of higher concentrations of silt, and eventually to the sandstone bedrock at ~125 m deep. It is reasonable to assume that similar sediment sequences occur in the 17th Drive segment (J. Elmo Rawling III, personal communication, 2020). My inferences for the 17th Drive segment are that the uppermost layer is a sandy outwash sediment, shown above the

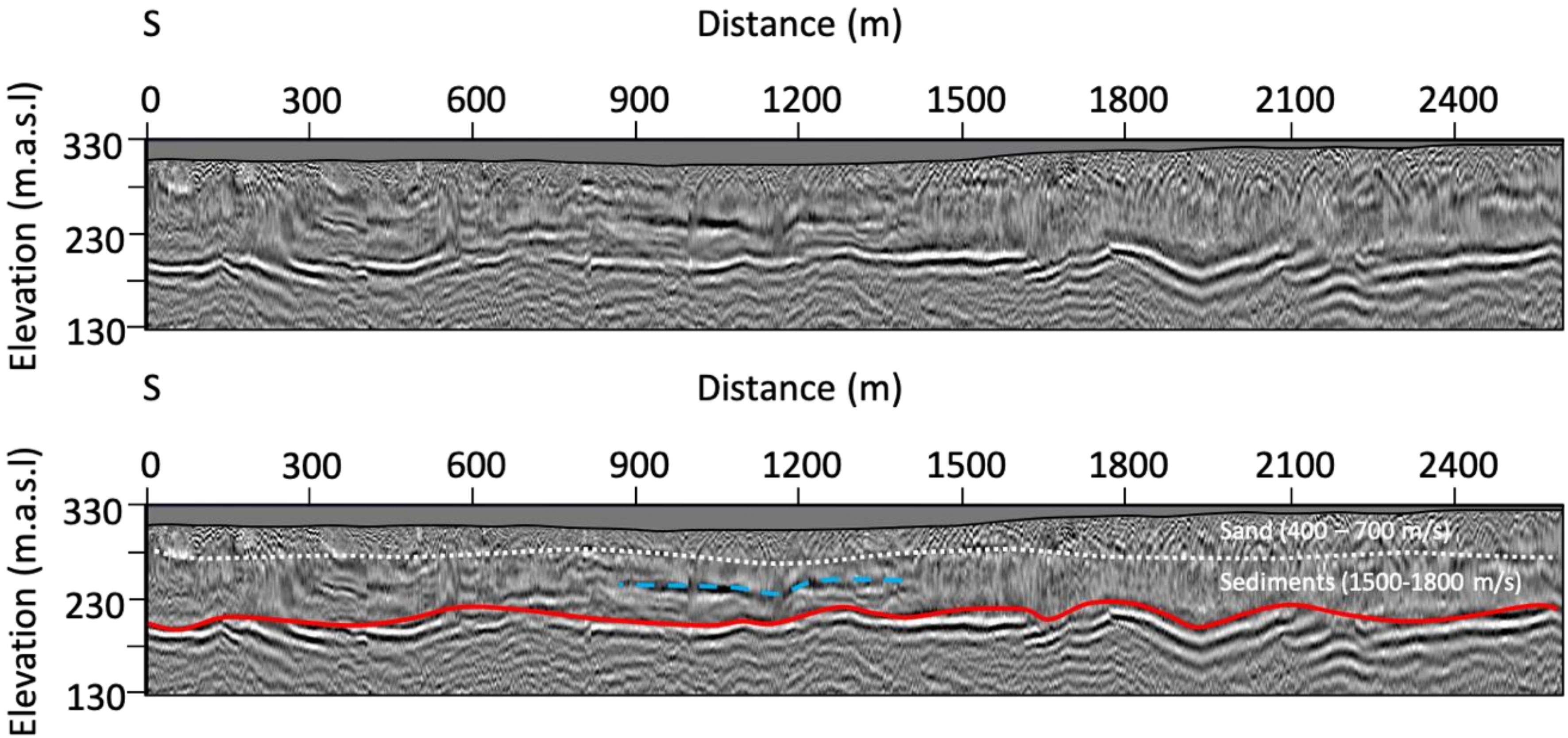

Figure 14. 17th Drive Cross-section. Processed seismic-reflection cross-section of the 17th Drive transect along the PTC. A) shows the processed data, whereas B) shows the interpretation of the sediment layers. The white dotted line delineates an upper layer of low velocity, mostly sandy sediment and a lower layer of higher velocity sediments. The red line shows the regional bedrock.

dotted white line in Figure 14, deposited on top of mostly sandy sediment with lenses containing larger concentrations of silt and clay. The sandy outwash sediments are underlain by the regional bedrock. The lenses of clay and silt could come from either aggradation of the moraine complex while the ice was at the Almond moraine position (J. Elmo Rawling III, personal communication, 2020) or potentially subglacial lake sediments, given the regional hydraulic potential discussed in section 5.2. I interpreted

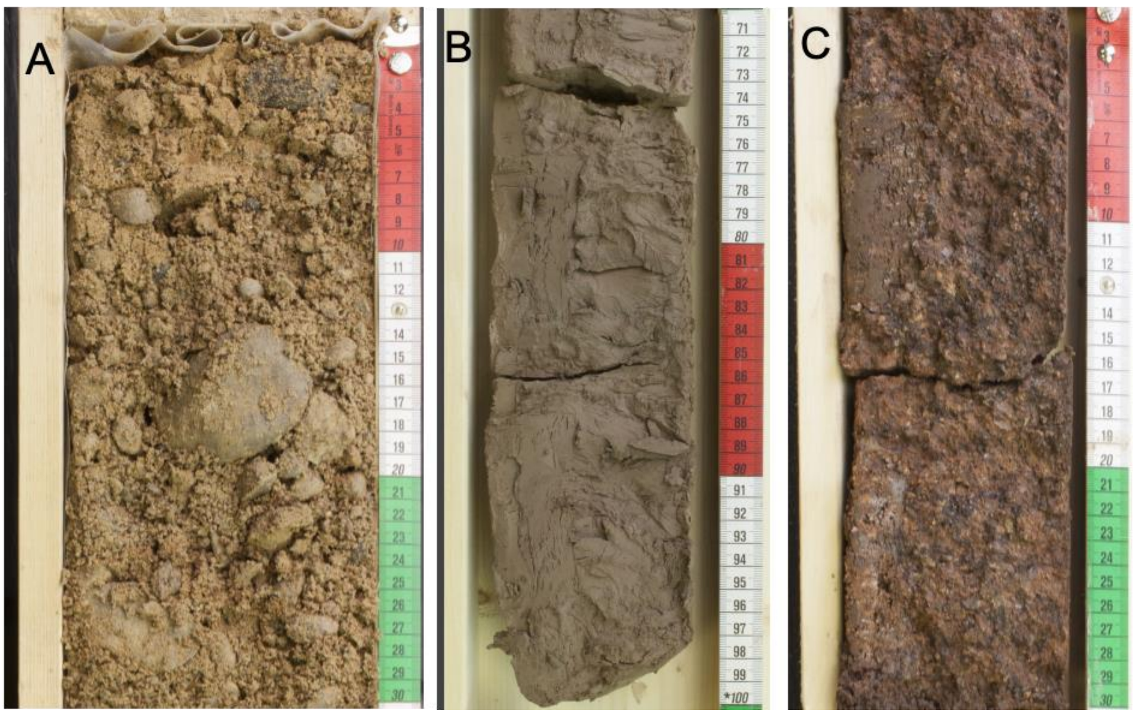

Figure 15. Sediment Core Log. Sediment core logs from the deep borehole done within the 11th Drive segment. Panel A shows sandy outwash ~15 meters deep. Panel B shows sediment with a larger silt/clay content ~ 40 meters deep. Panel C shows bedrock at the base of the core ~125 meters deep.

the shallow reflector in Figure 13, denoted by a blue dotted line, as one of these silt or clay packages. The ~40 m to ~50 m depth of the reflector is similar to the depth in the core log where sediments show high percentages of silt and clay. Additionally, the absence of the reflector beyond the ~ 500 m length identified in the cross-section shows that this reflector is not a larger regional feature, but a smaller anomaly in the subsurface.

I interpret the deeper reflector, denoted by the solid red line that spans the whole cross-section, to be the regional bedrock. The deeper reflector is at a depth of ~100 m to ~120 m, similar to that of the core log. I argue that the regional bedrock is likely sandstone due to the presence of sandstone in the core log at ~125 m depth. It is possible that portions of the interpreted bedrock are not sandstone. There are regional variations in thickness of the sandstone, so crystalline basement rock cannot be ruled out for at least portions of the section at 17th Drive. Additionally, it is possible that till packages exist overlying the regional bedrock, similar to the sometimes patchy and discontinuous tills observed in Iceland (Kjær et al., 2003). This distinction may be difficult, however, due to the generally high sand content of the till in this region (Syverson et al., 2011).

4.2 Subglacial Hydraulic-potential Model

The result of the subglacial hydraulic-potential modelling is shown in Figure 16. The light blue areas indicate potential subglacial lakes at the MIS-2 margin of the GBL, whereas the light red areas show potential subglacial lakes that could have drained through the PTC. In the entire model domain, 536 potential subglacial lakes were identified. The maximum and the minimum area for a single potential subglacial lake are 9.37 km^2 and 0.25 km^2, respectively. The mean area of potential subglacial lakes over the whole study area is 1.56 km^2. It is important to reiterate that the minimum threshold for a potential subglacial lake is 0.25 km^2. The total area of all of the potential subglacial lakes within the model domain is 837.60 km^2. The area up-ice from the PTC, shown in light red in Figure 16, shows an area of potential subglacial lakes, ~107 km^2 in total. This subset of the potential subglacial lakes is further discussed in section 5.2.

There are two important characteristics regarding the distribution of potential subglacial lakes in this region: 1) in the central lowland area, there are fewer potential subglacial lakes; and 2) the area surrounding the PTC exhibits a higher concentration of potential subglacial lakes compared to portions further south along the terminal moraine. This aligns with the previous analysis by Zoet et al. (2019) who showed that the higher concentration of potential subglacial lakes up-ice from the terminal moraine coincide with more TCs inferred in the modern topography.

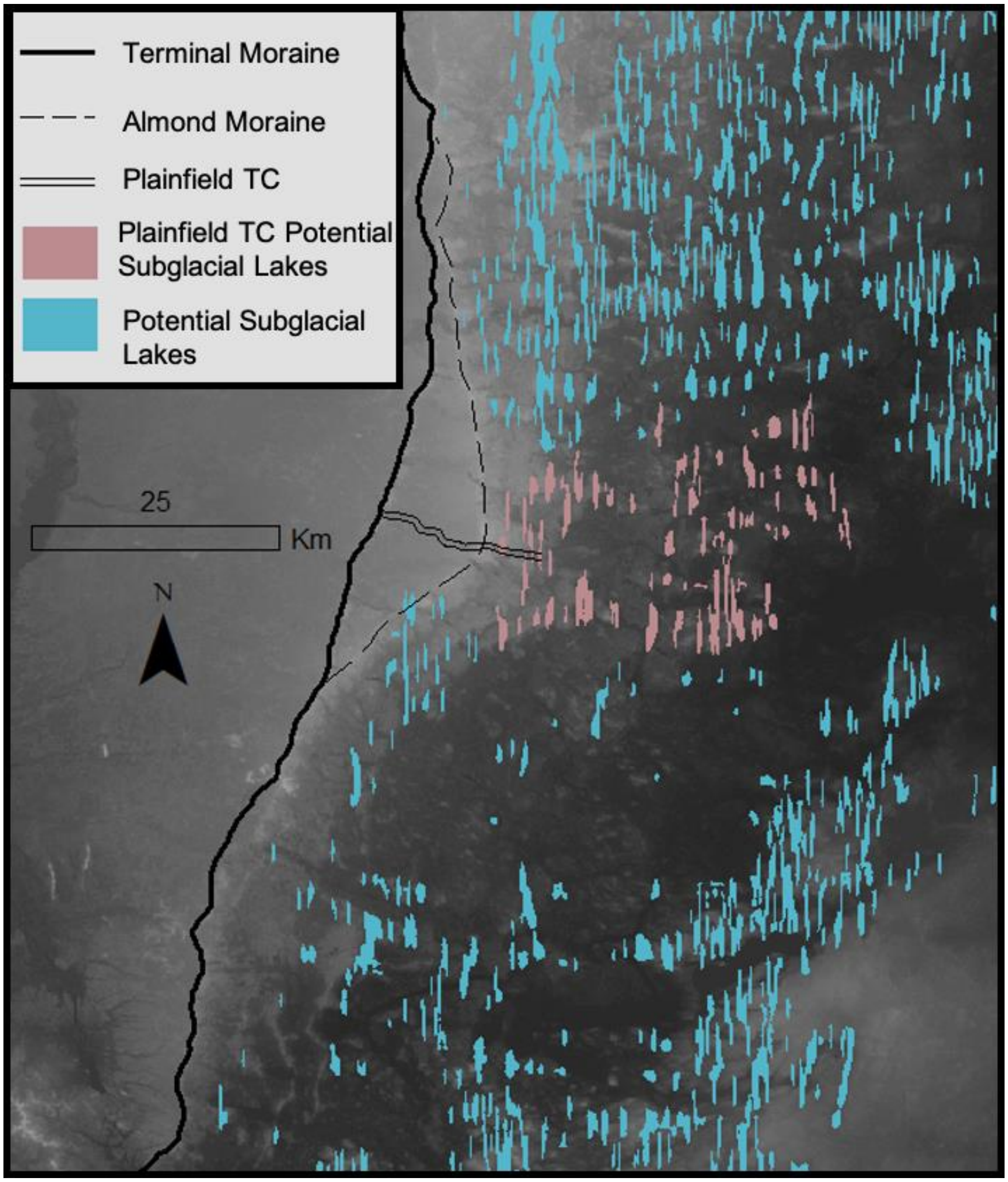

Figure 16. Potential Subglacial Lakes**.** Potential subglacial lake locations based on the divergence of the hydraulic-potential gradient. Potential subglacial lake locations are shown in light blue, with the light red denoting areas up-ice from the PTC. Terminal moraine is shown with a solid black line, the Almond moraine is shown with a dotted black line, and the PTC is shown with a pair of solid black lines. The base map is the SRTM digital elevation model.

CHAPTER 5

DISCUSSION

The absence of a channel feature on the seismic cross-section and the locations of potential subglacial lakes discussed in Chapter 4 provide insights into the formation of the PTC. In this chapter I will first discuss testing of my hypotheses. I will then discuss the relationship between the PTC and the regional hydraulic potential, which will include the identified potential subglacial lake locations and how they relate to channel incision. Next, I will discuss the modern topography and how this indicates where TCs are located. Then, I will analyze the role that supraglacial lakes likely played in the formation of the PTC. Finally, I will discuss how regional permafrost affects the ability for ice sheets to store subglacial water.

5.1 Hypothesis Testing

My first hypothesis was that the cross-sectional area of the PTC is smaller up-ice from the previously surveyed location at 11th Drive. Based on the lack of channel features in the reflection-seismic data across the 17th Drive transect (Figure 14), Hypothesis 1 is accepted. I then infer that the PTC initiates somewhere along the ~9.5 km path between the 11th and 17th Drive transects. One explanation for this is that the regional hydraulic potential changes from the 11th Drive section to the 17th Drive section. My second hypothesis was that the PTC formed over multiple drainage events with a substantial volume of supraglacial sources of water. Hypothesis 2 is also accepted due to the relatively smaller area of potential subglacial lakes, identified from the divergence of the hydraulic-potential gradient, compared to the estimate of Zoet et al. (2019).

5.2 Regional Hydraulic Potential and Subglacial Lake Area

There is no channel feature observed at the 17th Drive transect, which suggests that the channel initiates at some point between the 17th Drive transect and the 11th Drive transect along the PTC. Changes in the subglacial-water pressure and velocity likely caused this transition between a non-channelized region and the initiation of the PTC. Subglacial drainage via tunnel systems shows an inverse relationship between porewater pressure and the effective pressure (the overall pressure exerted on the bed) where an increase in effective pressure corresponds to a decrease in porewater pressure. Subsequently, this causes an increase in discharge through the subglacial conduits (Kamb, 1987). Water pressure directly relates to effective pressure in that a higher water pressure will counteract the weight of the overlying ice and decrease the effective pressure at that location (Hooke, 2005). Therefore, regions with higher water pressures, such as locations where subglacial lakes occur, would have a relatively lower discharge compared to the regions with lower water pressure. Differences in the hydraulic potential between locations, which drives changes in water pressure, could cause different velocities of water underneath the ice sheet. This gradient can be driven by large changes in subglacial bed slope (Hooke, 2005; Zoet et al., 2019).

My study region around 17th Drive exhibits a characteristically different bed slope compared to the previously studied region around 11th Drive. My study region shows a steeply dipping bed in the up-ice direction, whereas the 11th Drive region shows a relatively gently dipping bed down ice and toward the terminal moraine (Figure 2). Higher velocity sections, likely existing down-ice from the Almond margin in locations such as 11th Drive, would result in increased incision based on the model of the erosion rate (Carter et al., 2017; Zoet et al., 2019):

$$\dot{E} = K_1 \frac{V_s}{\alpha_{cc}} \left(\frac{\max(\tau_{cc} - \tau_k, 0)}{g(\rho_s - \rho_w) D_{15}} \right)^{\frac{3}{2}} \tag{2}$$

where K_1 is an erosion constant (Walder and Fowler, 1994), ρ_s is the sediment density, ρ_w is the water density, D_{15} is the 15th percentile grain size diameter, V_s is the settling velocity, τ_k is the critical shear stress value at the base of the channel, τ_{cc} is the channel bed shear stress, and α_{cc} is a channel geometry correction factor. The settling velocity in this equation relates to the velocity in the subglacial system, where an increase in velocity would correspond to an increase in erosion rate. Comparatively, a channel in lower velocity sections, likely existing up-ice from the Almond moraine, would incise less. This relationship is also true for subaerial settings (Walder and Fowler, 1994) and is an example of a positive feedback system where relatively high velocity, narrow channels show limited lateral erosion and would cause incision, whereas relatively low velocity, shallow channels would show limited incision and would result in lateral erosion (Wohl and Ikeda, 1997).

The total area of potential subglacial lakes that I calculated for the vicinity of the PTC is less than that estimated by Zoet et al. (2019). This discrepancy is due to the differences in the calculation methodology. My estimate is a more accurate representation of potential subglacial lakes due to the two-dimensional calculation of the hydraulic potential along with using the second derivative of the hydraulic potential. This area, shown in Figure 17, consists of 66 individual potential subglacial lakes, totaling ~107 km^2. Zoet et al. (2019), however, estimated that the subglacial area for water to pool is ~360 km^2, more than triple that of my estimate. Therefore, my lower estimate of potential subglacial lake area reinforces the conclusion of Zoet et al. (2019) that there was not enough subglacial water to form the PTC in one discharge event.

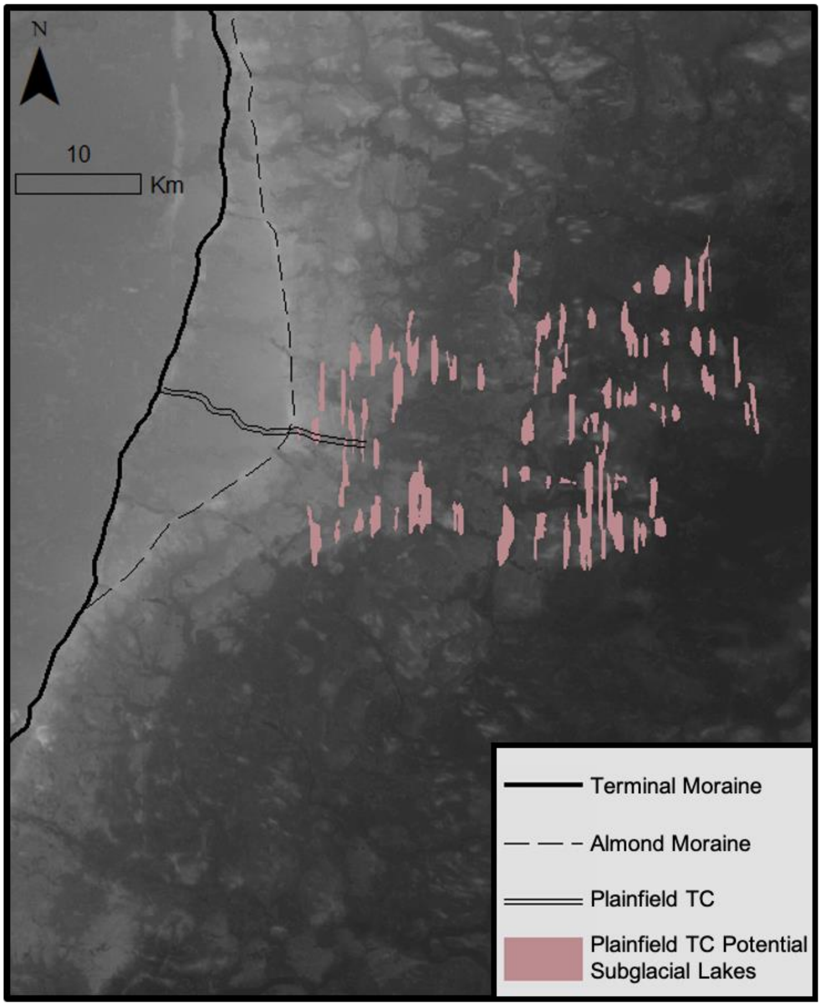

Figure 17. Potential PTC Subglacial Lakes. Potential subglacial lake areas around the general PTC location. The potential subglacial lake areas are shown in light red, whereas the Hancock moraine, Almond moraine, and PTC are shown as a solid line, dashed line, and double line, respectively. The base map is the SRTM digital elevation model

Alternatively, if I assume that a larger catchment area feeds into the PTC during a large subglacial drainage event, I can estimate an absolute maximum area for potential subglacial lakes. Using the total footprint (~8400 km^2) of the study area in Figure 16, instead of the focused area in Figure 17, the area for potential subglacial lakes is ~834 km^2, which is more than double the estimate of Zoet et al. (2019). Given the 5 km^3 of volume estimated to form the PTC (Zoet et al., 2019), the average depth of a subglacial lake would be ~6 m. This is a more realistic estimation compared to the ~14 m estimated by Zoet et al. (2019). However, it is unlikely that the entire area was able to fill and catastrophically drain simultaneously. In locations far north or south of the PTC, it is more likely that subglacial water present is going to flow parallel to ice flow and towards the terminal moraine in order to follow the gradient in the hydraulic potential (Hooke, 2005). Consequently, it is unlikely that the subglacial water would travel perpendicular to this flow path and intersect with the PTC. Because of this, it is likely that the total potential subglacial lake area estimate of ~107 km^2 is more accurate for the area around the PTC. Therefore, it is more likely that either several, short-duration discharge events occurred or there was substantial water volume input from supraglacial sources, or a combination of both.

5.3 Modern Surface Topography

Modern surface topography is used as an indicator for where these subglacial tunnel channels are located. Shown in Figure 5, the surface topography changes significantly between the 11th Drive and 17th Drive locations. The 11th Drive location and further down ice show a distinct channel-like feature with a surface depression and lakes forming within some of those depressions. On the other hand, around the 17th Drive transect, there is no clear depression based on the modern topography. This shows a lack of surficial evidence of a buried channel, where the topography variation is simply hummocky terrain due to moraine aggradation during the Almond phase of the LIS in this location. Based on the modern topography and the seismic cross-section showing the absence of a channel feature at 17^{th} Drive, I estimate that the Plainfield initiates 4-5 km down-ice from 17^{th} Drive, approximately 12-13 km up-ice from the terminal moraine. At this point, the hydraulic potential likely drives the subglacial water towards the terminus at sufficient speeds to cause incision. Comparing this location with the hydraulic potential model, it shows that some potential subglacial lake locations either coincide with or are down-ice from the PTC initiation location inferred from the modern topography. This could mean that either estimating the location of the initiation of the tunnel channel and its extent from the surface topography should not be the sole method of identifying tunnel channels, or that subglacial lakes can exist in locations that coincide with incised channels.

5.4 Supraglacial Lakes

Supraglacial lakes exist in both Greenland (e.g., Doyle et al., 2013; Fitzpatrick et al., 2014) and Antarctica (e.g., Langley et al., 2016; Stokes et al., 2019) and are an important source of water that can alter the effective pressure at the ice-bed interface after a drainage event (e.g., Bartholomew et al., 2012). Understanding their role in subglacial water drainage is an important aspect of understanding TC formation and how the fluctuation of effective pressure can alter the size and recurrence interval of subglacial lake drainage events. Previous studies have looked at supraglacial-lake distribution on both the Greenland Ice Sheet (GrIS) and the East Antarctic Ice Sheet (EAIS). Stokes et al. (2019) identified more than 65,000 supraglacial lakes on the margin of the EAIS, totaling more than 1,300 km^2 in area across the study area of ~5 million km^2. Generally, these lakes form at low elevations and shallow surface slopes, with ~60% of the identified lakes existing a few kilometers down-ice from the grounding line, located on ice shelves. Additionally, these lakes down-ice from the grounding line make up more than 80% of the total supraglacial lake area in the study. However, supraglacial lakes are identified as far as 500 km up-ice from the grounding line and do exist at high elevations. Similarly, Fitzpatrick et al. (2014) identified ~200 seasonally occurring supraglacial lakes across Russell Glacier in West Greenland. The mean area of a lake for any given year through the study period was 0.68 km^2. However, the maximum supraglacial-lake area in their dataset was 8.2 km^2. This gives an approximation on the order of hundreds of square kilometers of total supraglacial lake area across all lakes identified in the ~6500 km^2 study area, or just under two percent of the total area.

This contrast shows that Greenland, specifically West Greenland, is exhibiting a larger percentage of total supraglacial lake surface area across the ice surface compared to that of the East Antarctic margin. One possible explanation for this is that there is simply a study bias, since a majority of the supraglacial-lake studies focus on the GrIS, ice shelves, and the Antarctic Peninsula, while leaving out East Antarctica (Stokes et al., 2019). However, other studies argue that it is more likely there is simply less intense surface melt occurring and generally only exists at near-coastal regions (Trusel et al., 2012; Lenaerts et al., 2016). The cause of this can be attributed in part to the difference and changes in ocean and climate circulation in the Northern Hemisphere compared to the Southern Hemisphere and the lag time associated with global climate change. Previous studies have shown that the regional climate surrounding the Antarctic Ice Sheet

(AIS) and GrIS did not warm and cool simultaneously during past glacial and interglacial cycles (Crowley, 1992; Toggweiler and Lea, 2010). Leading up to LGM, between 47-23 ka before present, Antarctic climate changed prior to that of Greenland by an average of 1-2.5 ky. However, unlike the paleo-ice sheets, climate models predict that global warming will cause 1.7-2.0ºC of oceanic warming around Greenland compared to only 0.5-0.6ºC around Antarctica. Current observations show that Greenland ice mass loss is accelerating due to oceanic forcing (Bevis et al., 2019), and therefore likely better represents the behavior of the LIS during the Green Bay Lobe retreat out of modern-day Wisconsin.

Das et al. (2008) showed that water-driven fracture propagation beneath supraglacial lakes transports large volumes of supraglacially-stored water to the bed of the GrIS. Fitzpatrick et al. (2014) showed that for Russell Glacier in West Greenland, supraglacial lakes drain rapidly (<4 days) only ~28% of the time. However, when drainage events do occur, they facilitate regional, transient ice-sheet acceleration (Das et al. 2008, Doyle et al. 2013, Tedesco et al. 2013). Additionally, the propagation of these conduits from hydraulic fracturing creates pathways, or moulins, for water to follow for the remainder of the melt season (Joughin et al., 2008; Jougin et al., 2013; Andrews et al., 2014). On the GrIS, moulins often form away from heavily crevassed zones, further up-ice (Yang & Smith 2016). However, when an ice-sheet model is forced to replicate surface velocities that match GPS observations, the surface-parallel Von Mises stresses predicted are insufficient to replicate the moulin formations observed (Hoffman et al. 2018). The ice-sheet model shows that moulins are replicated near large volumes of supraglacial meltwater that catastrophically drain to the bed, showing that the distribution of moulins is closely tied to supraglacial lake drainage events (Hoffman et al. 2018).

Stevens et al. (2015) argues that the trigger mechanism for these supraglacial lake drainage events is the ice-sheet uplift and/or enhanced basal slip. Additionally, Stevens et al. (2015) argues that further towards the ice-sheet interior, where there is less water at the bed, these hydraulic-fracture lake-drainage events are likely less pervasive. This same reasoning could explain why there are more tunnel channels on the western side of the Green Bay Lobe of the LIS, where subglacial lakes likely formed at locations ~ 15-20 km up-ice from the terminal moraine in this region. When these lakes fill, they perturb the hydraulic equilibrium between the basal water pressure and that from the overburden ice, thereby reducing the effective pressure above these subglacial lakes (Wingham et al., 2006). This would cause regional ice uplift and/or ice velocity increases which could propagate hydraulic fracturing and drain any supraglacial lakes in the region. Even with this additional water source, the overall volume of water is insufficient to produce the PTC in one drainage event, and therefore it is unlikely that tunnel channels as a whole are formed from one drainage event. This means supraglacial lakes do influence the formation of tunnel channels by supplying water to the ice-sheet bed during drainage events, but multiple drainage events occur over the course of one or multiple melt seasons and carve tunnel channels.

5.5 Permafrost

Other geologic factors, such as permafrost, likely play a role in the formation of the PTC by indirectly assisting the storage of water. Periglacial permafrost extending into the driftless area of Wisconsin has been inferred from ice-wedge polygon and ice-wedge cast features (Clayton et al. 2001). These features only form within permafrost and act as a tracer for the extent of permafrost in a region. Additional evidence for the persistence of permafrost in this region comes from speleothem analysis by Batchelor et al. (2019) from within a cave in the driftless area. Based on the age of growth layers of the speleothems in this cave, they infer that while permafrost was present in the region growth from limestone precipitation would not occur. They estimate permafrost persisted in this area until ~15 ka. Additionally, Rawling and Attig (2018) estimated permafrost remained in the Northern Highlands region of Wisconsin until about 13-14 ka. This regional permafrost helps facilitate pooling of water behind the terminal moraine and effectively acts as a seal, trapping subglacial water (Attig et al., 1989; Cutler et al., 2002; Zoet et al. 2019). When a subglacial drainage event occurs, initially the ice lifts from the bed as porewater pressure increases and is decoupled from the permafrost near the terminus (Das et al., 2008). Subsequently, as the TC forms and drainage proceeds, the traction at the bed increases so that after the drainage event the overall resistance to ice flow is higher than just prior to the event (Zoet et al. 2019). This additional traction at the bed acts to re-seal the permafrost/ice boundary and further facilitates pooling of water behind the terminal moraine (Zoet et al. 2019). This likely occurs periodically while the ice sheet is at the terminal margin and permafrost exists beyond this margin and into the periglacial environment.

CHAPTER 6

CONCLUSIONS

The active-seismic reflection survey reveals that there is no subsurface channel present at the 17th Drive transect of the Plainfield tunnel channel (PTC). It is then inferred that the PTC initiates at some distance down-ice from the 17th Drive transect, then increases in cross-section area prior to the 11th Drive transect. This phenomenon can be explained by the regional hydraulic potential, where at 17th Drive subglacial water likely pooled locally. However, at 11th Drive it is likely that little to no subglacial-water pooling occurred, and instead channel incision happens due to the positive bed slope gradient towards the terminal moraine, where a relatively faster-flowing water around this location carved the tunnel channel over time.

Supraglacial lakes likely have a large influence on the TC formation in this region. As the TC formation progresses, subglacial traction increases due to the porewater draining into the TC from the surrounding sediments, resulting in local ice thickening. This in turn leads to supraglacial lake formation up-ice from this region of local ice thickening. Water from these supraglacial lakes subsequently drive future drainage events. When supraglacial lakes drain through moulins, over-pressurization of the water at the ice-bed interface could occur and drive a subsequent subglacial outburst flooding event, which likely further incised the PTC.

REFERENCES CITED

Anderson, R. S., & Anderson, S. P. (2010). *Geomorphology: The Mechanics and Chemistry of Landscapes*. Cambridge University Press.

Andrews, L. C., Catania, G. A., Hoffman, M. J., Gulley, J. D., Lüthi, M. P., Ryser, C., … Neumann, T. A. (2014). Direct observations of evolving subglacial drainage beneath the Greenland Ice Sheet. *Nature*, *514*(7520), 80–83. https://doi.org/10.1038/nature13796

Attig, J. W., Mickelson, D. M., & Clayton, L. (1989). Late Wisconsin landform distribution and glacier-bed conditions in Wisconsin. *Sedimentary Geology*, *62*(2), 399–405. https://doi.org/https://doi.org/10.1016/0037-0738(89)90128-0

Attig, J. W., & Rawling III, J. E. (2018). Influence of persistent buried ice on late glacial landscape development in part of Wisconsin's Northern Highlands. (A. E. Kehew & B. B. Curry, Eds.), *Quaternary Glaciation of the Great Lakes Region: Process, Landforms, Sediments, and Chronology*. Geological Society of America. https://doi.org/10.1130/2017.2530(05)

Baker, G. S. (1999). Processing Near-Surface Seismic Reflection Data: A Primer. Society of Exploration Geophysicists. https://doi.org/10.1190/1.9781560802020

Bartholomaus, T. C., Anderson, R. S., & Anderson, S. P. (2008). Response of glacier basal motion to transient water storage. *Nature Geoscience*, *1*(1), 33–37. https://doi.org/10.1038/ngeo.2007.52

Bartholomew, I., Nienow, P., Mair, D., Hubbard, A., King, M. A., & Sole, A. (2010). Seasonal evolution of subglacial drainage and acceleration in a Greenland outlet glacier. *Nature Geoscience*, *3*(6), 408–411. https://doi.org/10.1038/ngeo863

Bartholomew, I., Nienow, P., Sole, A., Mair, D., Cowton, T., and King, M. A. (2012), Short-term variability in Greenland Ice Sheet motion forced by time-varying meltwater drainage: Implications for the relationship between subglacial drainage system behavior and ice velocity, *J. Geophys. Res.*, 117, F03002, doi:10.1029/2011JF002220.

Batchelor, C. J., Orland, I. J., Marcott, S. A., Slaughter, R., Edwards, R. L., Zhang, P., … Cheng, H. (2019). Distinct Permafrost Conditions Across the Last Two Glacial Periods in Midlatitude North America. *Geophysical Research Letters*, *46*(22), 13318–13326. https://doi.org/10.1029/2019GL083951

Bevis, M., Harig, C., Khan, S. A., Brown, A., Simons, F. J., Willis, M., … Nylen, T. (2019). Accelerating changes in ice mass within Greenland, and the ice sheet's sensitivity to atmospheric forcing. *Proceedings of the National Academy of Sciences*, *116*(6), 1934 LP – 1939. https://doi.org/10.1073/pnas.1806562116

Carter, S. P., Fricker, H. A., & Siegfried, M. R. (2017). Antarctic subglacial lakes drain through sediment-floored canals: Theory and model testing on real and idealized domains. *Cryosphere*, *11*(1), 381–405. https://doi.org/10.5194/tc-11-381-2017

Clark, P. U. (1992). Surface form of the southern Laurentide Ice Sheet and its implications to ice-sheet dynamics. *GSA Bulletin*, *104*(5), 595–605. https://doi.org/10.1130/0016-7606(1992)104<0595:SFOTSL>2.3.CO;2

Clayton, L., Attig, J. W., & Mickelson, D. M. (1999). Tunnel channels formed in Wisconsin during the last glaciation. In D. M. Mickelson & J. W. Attig (Eds.), *Glacial Processes Past and Present* (Vol. 337, p. 0). Geological Society of America. https://doi.org/10.1130/0-8137-2337-X.69

Clayton, L., Attig, J. W., & Mickelson, D. M. (2001). Effects of late Pleistocene permafrost on the landscape of Wisconsin, USA. *Boreas*, *30*(3), 173–188. https://doi.org/10.1111/j.1502-3885.2001.tb01221.x

Colgan, P. M. (1999). Reconstruction of the Green Bay Lobe, Wisconsin, United States from 26,000 to 13,000 radiocarbon years B.P. In D. M. Mickelson & J. W. Attig (Eds.), *Glacial Processes Past and Present* (Vol. 337, p. 0). Geological Society of America. https://doi.org/10.1130/0-8137-2337-X.137

Crowley, T. J. (1992). North Atlantic Deep Water cools the southern hemisphere. *Paleoceanography*, *7*(4), 489–497. https://doi.org/10.1029/92PA01058

Cutler, P. M., Colgan, P. M., & Mickelson, D. M. (2002). Sedimentologic evidence for outburst floods from the Laurentide Ice Sheet margin in Wisconsin, USA: implications for tunnel-channel formation. *Quaternary International*, *90*(1), 23–40. https://doi.org/https://doi.org/10.1016/S1040-6182(01)00090-8

Das, S. B., Joughin, I., Behn, M. D., Howat, I. M., King, M. A., Lizarralde, D., & Bhatia, M. P. (2008). Fracture Propagation to the Base of the Greenland Ice Sheet During Supraglacial Lake Drainage. *Science*, *320*(5877), 778 LP – 781. https://doi.org/10.1126/science.1153360

Doyle, S. H., Hubbard, A. L., Dow, C. F., Jones, G. A., Fitzpatrick, A., Gusmeroli, A., … Box, J. E. (2013). Ice tectonic deformation during the rapid in situ drainage of a supraglacial lake on the Greenland Ice Sheet. *The Cryosphere, 7*(1), 129–140. https://doi.org/10.5194/tc-7-129-2013

Fitzpatrick, A. A. W., Hubbard, A. L., Box, J. E., Quincey, D. J., van As, D., Mikkelsen, A. P. B., … Jones, G. A. (2014). A decade (2002-2012) of supraglacial lake volume estimates across Russell Glacier, West Greenland. *The Cryosphere*, *8*(1), 107–121. https://doi.org/10.5194/tc-8-107-2014

Flowers, G. E. (2015). Modelling water flow under glaciers and ice sheets. *Proceedings of the Royal Society A: Mathematical, Physical and Engineering Sciences*. The Royal Society. https://doi.org/10.1098/rspa.2014.0907

Fountain, A. G., & Walder, J. S. (1998). Water flow through temperate glaciers. *Reviews of Geophysics*, *36*(3), 299–328. https://doi.org/10.1029/97RG03579

Fricker, H. A., Scambos, T., Bindschadler, R., & Padman, L. (2007). An Active Subglacial Water System in West Antarctica Mapped from Space. *Science*, *315*(5818), 1544 LP – 1548. https://doi.org/10.1126/science.1136897

Fricker, H. A., & Scambos, T. (2009). Connected subglacial lake activity on lower Mercer and Whillans Ice Streams, West Antarctica, 2003–2008. *Journal of Glaciology*, *55*(190), 303–315. https://doi.org/DOI: 10.3189/002214309788608813

Goodwin, I. D. (1988). The Nature and Origin of a Jökulhlaup Near Casey Station, Antarctica. *Journal of Glaciology*, *34*(116), 95–101. https://doi.org/DOI: 10.3189/S0022143000009114

Gordon, S., Sharp, M., Hubbard, B., Smart, C., Ketterling, B., & Willis, I. (1998). Seasonal reorganization of subglacial drainage inferred from measurements in boreholes. *Hydrological Processes*, *12*(1), 105–133. https://doi.org/10.1002/(SICI)1099-1085(199801)12:1<105::AID-HYP566>3.0.CO;2-#

Hoffman, M. J., Perego, M., Andrews, L. C., Price, S. F., Neumann, T. A., Johnson, J. V, … Lüthi, M. P. (2018). Widespread Moulin Formation During Supraglacial Lake Drainages in Greenland. *Geophysical Research Letters*, *45*(2), 778–788. https://doi.org/10.1002/2017GL075659

Hooke, R. L. (2005). *Principles of Glacier Mechanics* (2nd ed.). Cambridge: Cambridge University Press. https://doi.org/DOI: 10.1017/CBO9780511614231

Iken, A., & Bindschadler, R. A. (1986). Combined measurements of Subglacial Water Pressure and Surface Velocity of Findelengletscher, Switzerland: Conclusions about Drainage System and Sliding Mechanism. *Journal of Glaciology*, *32*(110), 101–119. https://doi.org/DOI: 10.3189/S0022143000006936

Jansson, P. (1995). Water pressure and basal sliding on Storglaciären, northern Sweden. *Journal of Glaciology*, *41*(138), 232–240. https://doi.org/DOI: 10.3189/S0022143000016130

Joughin, I., Das, S. B., King, M. A., Smith, B. E., Howat, I. M., & Moon, T. (2008). Seasonal Speedup Along the Western Flank of the Greenland Ice Sheet. *Science*, *320*(5877), 781 LP – 783. https://doi.org/10.1126/science.1153288

Joughin, I., Das, S. B., Flowers, G. E., Behn, M. D., Alley, R. B., King, M. A., … van Angelen, J. H. (2013). Influence of ice-sheet geometry and supraglacial lakes on seasonal ice-flow variability. *The Cryosphere*, *7*(4), 1185–1192. https://doi.org/10.5194/tc-7-1185-2013

Kamb, B. (1987). Glacier surge mechanism based on linked cavity configuration of the basal water conduit system. *Journal of Geophysical Research: Solid Earth*, *92*(B9), 9083–9100. https://doi.org/10.1029/JB092iB09p09083

Kjær, K. H., Krüger, J., & van der Meer, J. J. M. (2003). What causes till thickness to change over distance? Answers from Mýrdalsjökull, Iceland. *Quaternary Science Reviews*, *22*(15), 1687–1700. https://doi.org/https://doi.org/10.1016/S0277-3791(03)00162-8

Langley, E. S., Leeson, A. A., Stokes, C. R., & Jamieson, S. S. R. (2016). Seasonal evolution of supraglacial lakes on an East Antarctic outlet glacier. *Geophysical Research Letters*, *43*(16), 8563–8571. https://doi.org/10.1002/2016GL069511

Lenaerts, J. T. M., Vizcaino, M., Fyke, J., van Kampenhout, L., & van den Broeke, M. R. (2016). Present-day and future Antarctic ice sheet climate and surface mass balance in the Community Earth System Model. *Climate Dynamics*, *47*(5), 1367–1381. https://doi.org/10.1007/s00382-015-2907-4

Livingstone, S. J., & Clark, C. D. (2016). Morphological properties of tunnel valleys of the southern sector of the Laurentide Ice Sheet and implications for their formation. *Earth Surf. Dynam.*, *4*(3), 567–589. https://doi.org/10.5194/esurf-4-567-2016

Lliboutry, L. (1976). Physical Processes in Temperate Glaciers. *Journal of Glaciology*, *16*(74), 151–158. https://doi.org/DOI: 10.3189/S002214300003149X

Margold, M., Stokes, C. R., & Clark, C. D. (2015). Ice streams in the Laurentide Ice Sheet: Identification, characteristics and comparison to modern ice sheets. *Earth-Science Reviews*, *143*, 117–146. https://doi.org/https://doi.org/10.1016/j.earscirev.2015.01.011

Meierbachtol, T., Harper, J., & Humphrey, N. (2013). Basal Drainage System Response to Increasing Surface Melt on the Greenland Ice Sheet. *Science*, *341*(6147), 777–779. https://doi.org/10.1126/science.1235905

Moores, H. D. (1989). On the formation of the tunnel valleys of the Superior lobe, central Minnesota. *Quaternary Research*, *32*(1), 24–35. https://doi.org/https://doi.org/10.1016/0033-5894(89)90029-X

Murray, T., & Clarke, G. K. C. (1995). Black-box modeling of the subglacial water system. *Journal of Geophysical Research: Solid Earth*, *100*(B6), 10231–10245. https://doi.org/10.1029/95JB00671

Popov, S. V, & Masolov, V. N. (2007). Forty-seven new subglacial lakes in the 0–110° E sector of East Antarctica. *Journal of Glaciology*, *53*(181), 289–297. https://doi.org/DOI: 10.3189/172756507782202856

Pugin, A., Pullan, S. E., & Sharpe, D. R. (1996). Observations of tunnel channels in glacial sediments with shallow land-based seismic reflection. *Annals of Glaciology*, *22*, 176–180. https://doi.org/10.3189/1996AoG22-1-176-180

Pugin, A. J.-M., Pullan, S. E., Hunter, J. A., & Oldenborger, G. A. (2009). Hydrogeological prospecting using P- and S-wave landstreamer seismic reflection methods. *Near Surface Geophysics*, *7*(5–6), 315–328. https://doi.org/10.3997/1873-0604.2009033

Sergienko, O. V. (2013). Glaciological twins: basally controlled subglacial and supraglacial lakes. *Journal of Glaciology*, *59*(213), 3–8. https://doi.org/DOI: 10.3189/2013JoG12J040

Shackleton, C., Patton, H., Hubbard, A., Winsborrow, M., Kingslake, J., Esteves, M., … Greenwood, S. L. (2018). Subglacial water storage and drainage beneath the Fennoscandian and Barents Sea ice sheets. *Quaternary Science Reviews*, *201*, 13–28. https://doi.org/https://doi.org/10.1016/j.quascirev.2018.10.007

Shreve, R. L. (1972). Movement of Water in Glaciers. *Journal of Glaciology*, *11*(62), 205–214. https://doi.org/DOI: 10.3189/S002214300002219X

Siegert, M. J. (2000). Antarctic subglacial lakes. *Earth-Science Reviews*, *50*(1), 29–50. https://doi.org/https://doi.org/10.1016/S0012-8252(99)00068-9

Siegfried, M. R., Fricker, H. A., Carter, S. P., & Tulaczyk, S. (2016). Episodic ice velocity fluctuations triggered by a subglacial flood in West Antarctica. *Geophysical Research Letters*, *43*(6), 2640–2648. https://doi.org/10.1002/2016GL067758

Smith, B. E., Gourmelen, N., Huth, A., & Joughin, I. (2017). Connected subglacial lake drainage beneath Thwaites Glacier, West Antarctica. *The Cryosphere*, *11*(1), 451–467. https://doi.org/10.5194/tc-11-451-2017

Stearns, L. A., Smith, B. E., & Hamilton, G. S. (2008). Increased flow speed on a large east antarctic outlet glacier caused by subglacial floods. *Nature Geoscience*. Nature Publishing Group. https://doi.org/10.1038/ngeo356

Stevens, L. A., Behn, M. D., McGuire, J. J., Das, S. B., Joughin, I., Herring, T., … King, M. A. (2015). Greenland supraglacial lake drainages triggered by hydrologically induced basal slip. *Nature*, *522*(7554), 73–76. https://doi.org/10.1038/nature14480

Stokes, C. R., Sanderson, J. E., Miles, B. W. J., Jamieson, S. S. R., & Leeson, A. A. (2019). Widespread distribution of supraglacial lakes around the margin of the East Antarctic Ice Sheet. *Scientific Reports*, *9*(1), 13823. https://doi.org/10.1038/s41598-019-50343-5

Sundal, A. V., Shepherd, A., Nienow, P., Hanna, E., Palmer, S., & Huybrechts, P. (2011). Melt-induced speed-up of Greenland ice sheet offset by efficient subglacial drainage. *Nature*, *469*(7331), 521–524. https://doi.org/10.1038/nature09740

Syverson, K.M., Colgan, P.M., 2011. The Quaternary of Wisconsin: an updated review of stratigraphy, glacial history and landforms. In: Ehlers, J., Gibbard, P.L., Hughes, P.D. (Eds.), *Quaternary Glaciations—Extent and Chronology: A Closer Look*. Developments in Quaternary Sciences 15. Elsevier, Amsterdam, pp. 537–552.

Tedesco, M., Willis, I. C., Hoffman, M. J., Banwell, A. F., Alexander, P., & Arnold, N. S. (2013). Ice dynamic response to two modes of surface lake drainage on the Greenland ice sheet. *Environmental Research Letters*, *8*(3), 34007. https://doi.org/10.1088/1748-9326/8/3/034007

Thomason, J.F., Larson, T.R., Ismail, A., & Sargent, S., (2018). Characterizing glacial sediments and features in northeast Illinois using electrical resistivity and seismic-reflection profiling. (A. E. Kehew & B. B. Curry, Eds.), *Quaternary Glaciation of the Great Lakes Region: Process, Landforms, Sediments, and Chronology*. 530, p. 233. https://doi.org/10.1130/2018.2530(12)

Thwaites, F. T. (1943). Pleistocene of part of northeastern Wisconsin. *GSA Bulletin*, *54*(1), 87–144. https://doi.org/10.1130/GSAB-54-87

Toggweiler, J. R., & Lea, D. W. (2010). Temperature differences between the hemispheres and ice age climate variability. *Paleoceanography*, *25*(2). https://doi.org/10.1029/2009PA001758

Trusel, L. D., Frey, K. E., & Das, S. B. (2012). Antarctic surface melting dynamics: Enhanced perspectives from radar scatterometer data. *Journal of Geophysical Research: Earth Surface*, *117*(F2). https://doi.org/10.1029/2011JF002126

Walder, J. S., & Fowler, A. (1994). Channelized subglacial drainage over a deformable bed. *Journal of Glaciology*, *40*(134), 3–15. https://doi.org/DOI: 10.3189/S0022143000003750

Wingham, D. J., Siegert, M. J., Shepherd, A., & Muir, A. S. (2006). Rapid discharge connects Antarctic subglacial lakes. *Nature*, *440*(7087), 1033–1036. https://doi.org/10.1038/nature04660

Wohl, E., & Ikeda, H. (1997). Experimental simulation of channel incision into a cohesive substrate at varying gradients. *Geology*, *25*(4), 295–298. https://doi.org/10.1130/0091-7613(1997)025<0295:ESOCII>2.3.CO;2

Wright, A., & Siegert, M. (2012). A fourth inventory of Antarctic subglacial lakes. *Antarctic Science*, *24*(06), 659–664. https://doi.org/10.1017/S095410201200048X

Yang, K., & Smith, L. C. (2016). Internally drained catchments dominate supraglacial hydrology of the southwest Greenland Ice Sheet. *Journal of Geophysical Research: Earth Surface*, *121*(10), 1891–1910. https://doi.org/10.1002/2016JF003927

Zoet, L. K., Muto, A., Rawling, J. E., & Attig, J. W. (2019). The effects of tunnel channel formation on the Green Bay Lobe, Wisconsin, USA. *Geomorphology*, *324*, 36–47. https://doi.org/https://doi.org/10.1016/j.geomorph.2018.09.021

APPENDIX A

SUPPLEMENTARY FIGURES

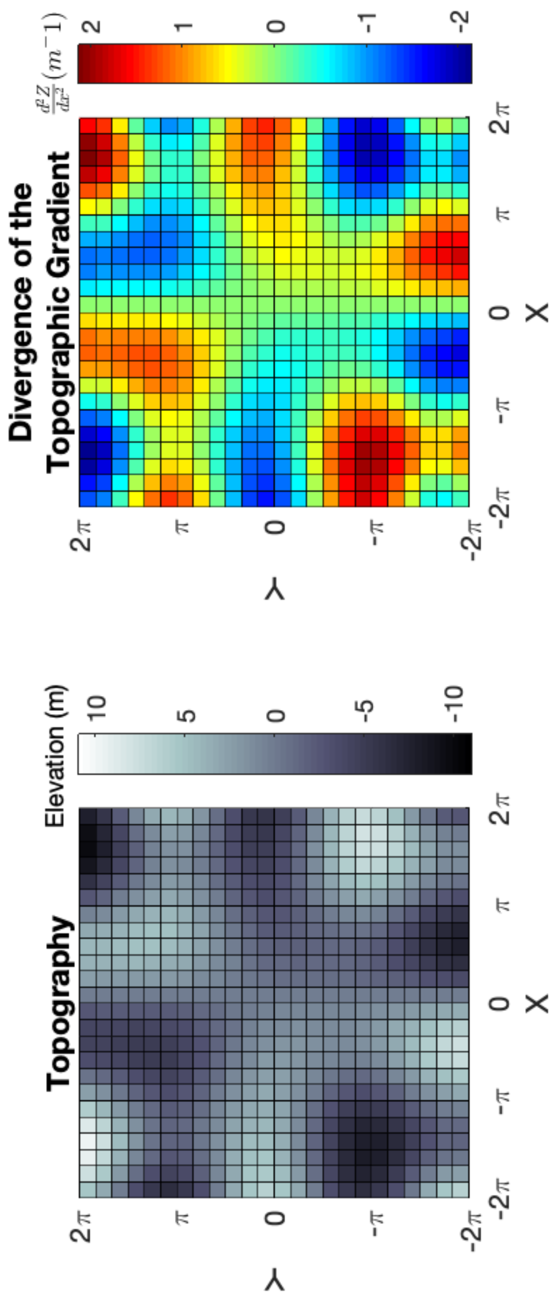

Figure A1. Divergence Calculation. The topography is produced with a simple function $Z = Y * \sin(X) - X * \cos(Y)$ with X and Y ranging from -2π to 2π. The Divergence of the Topographic Gradient is the second derivative of the topography.

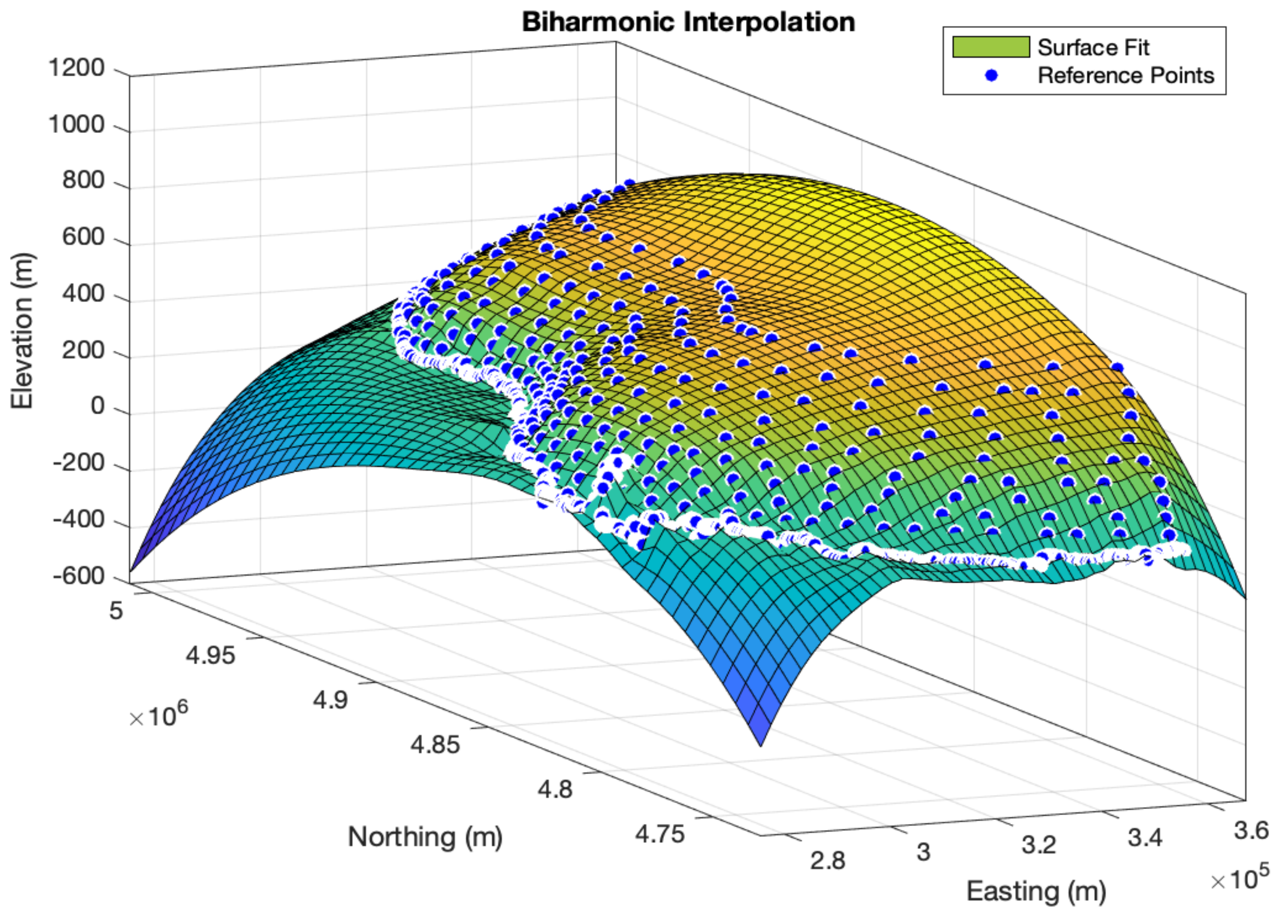

Figure A2: Biharmonic interpolation method ice-surface fit. Reference points correspond to the equal-elevation lines from Clark 1992. Viewpoint is looking Northeast in the up-ice direction.

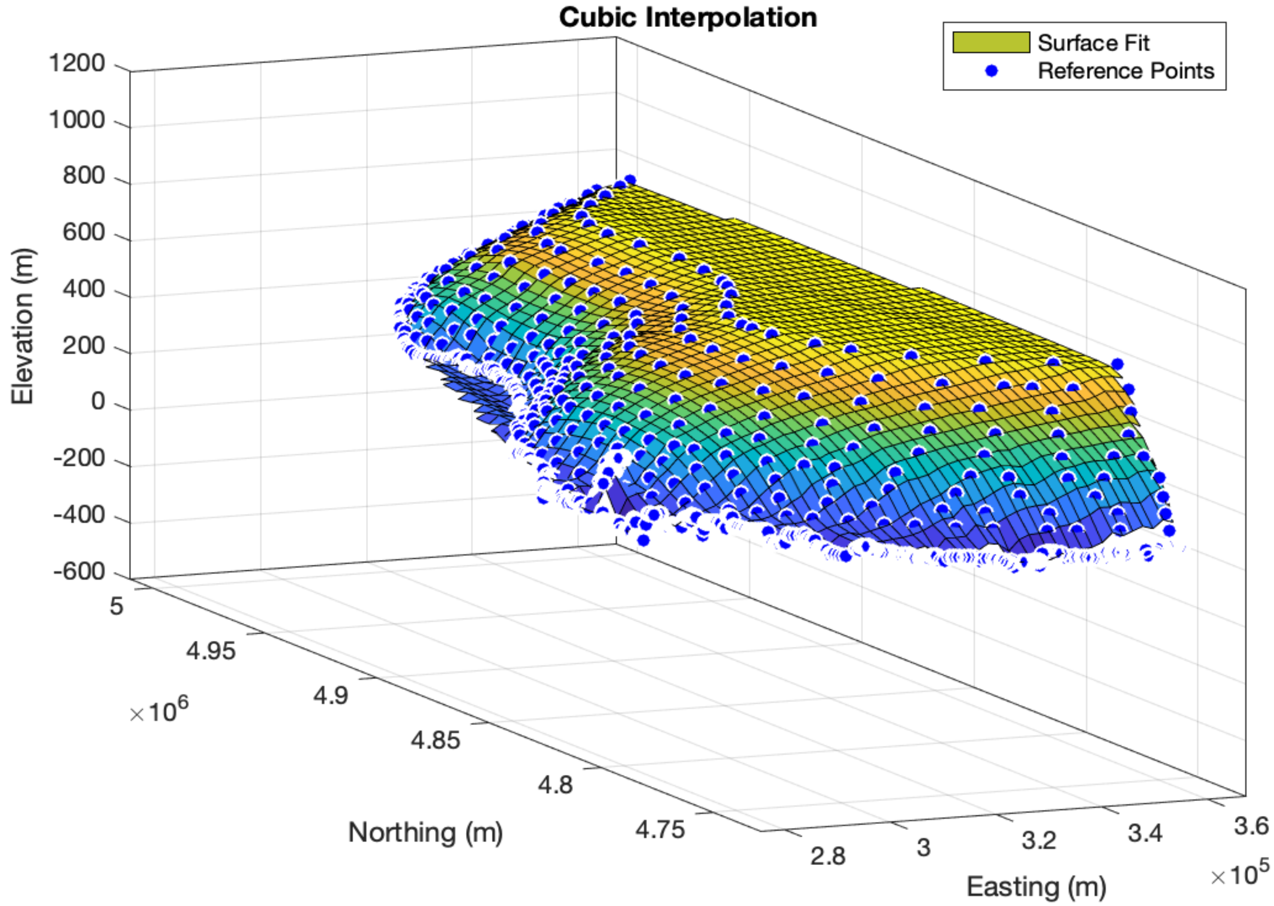

Figure A3. Cubic spline interpolation method ice-surface fit. Reference points correspond to the equal-elevation lines from Clark 1992. Viewpoint is looking Northeast in the up-ice direction.

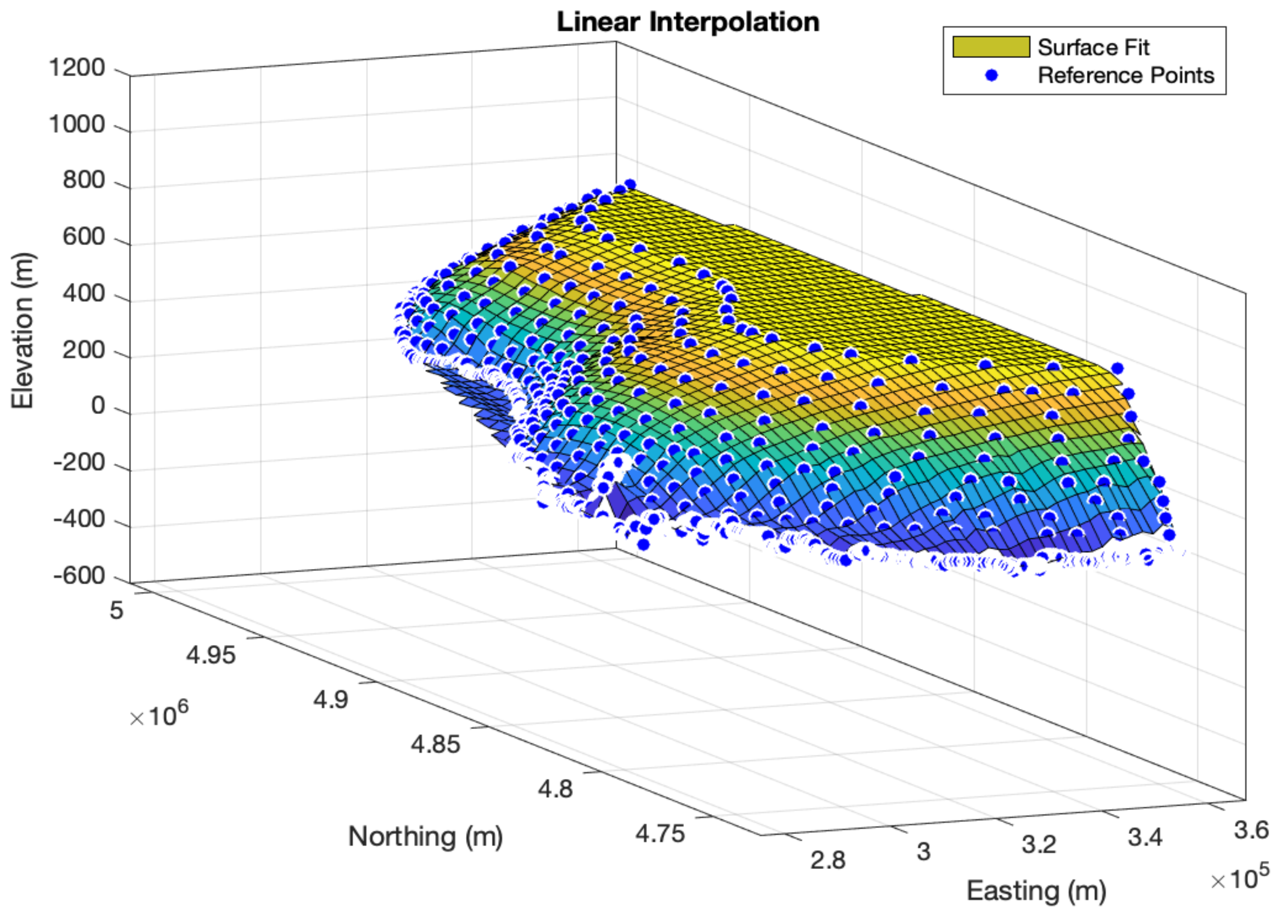

Figure A4. Linear interpolation method ice-surface fit. Reference points correspond to the equal-elevation lines from Clark 1992. Viewpoint is looking Northeast in the up-ice direction.

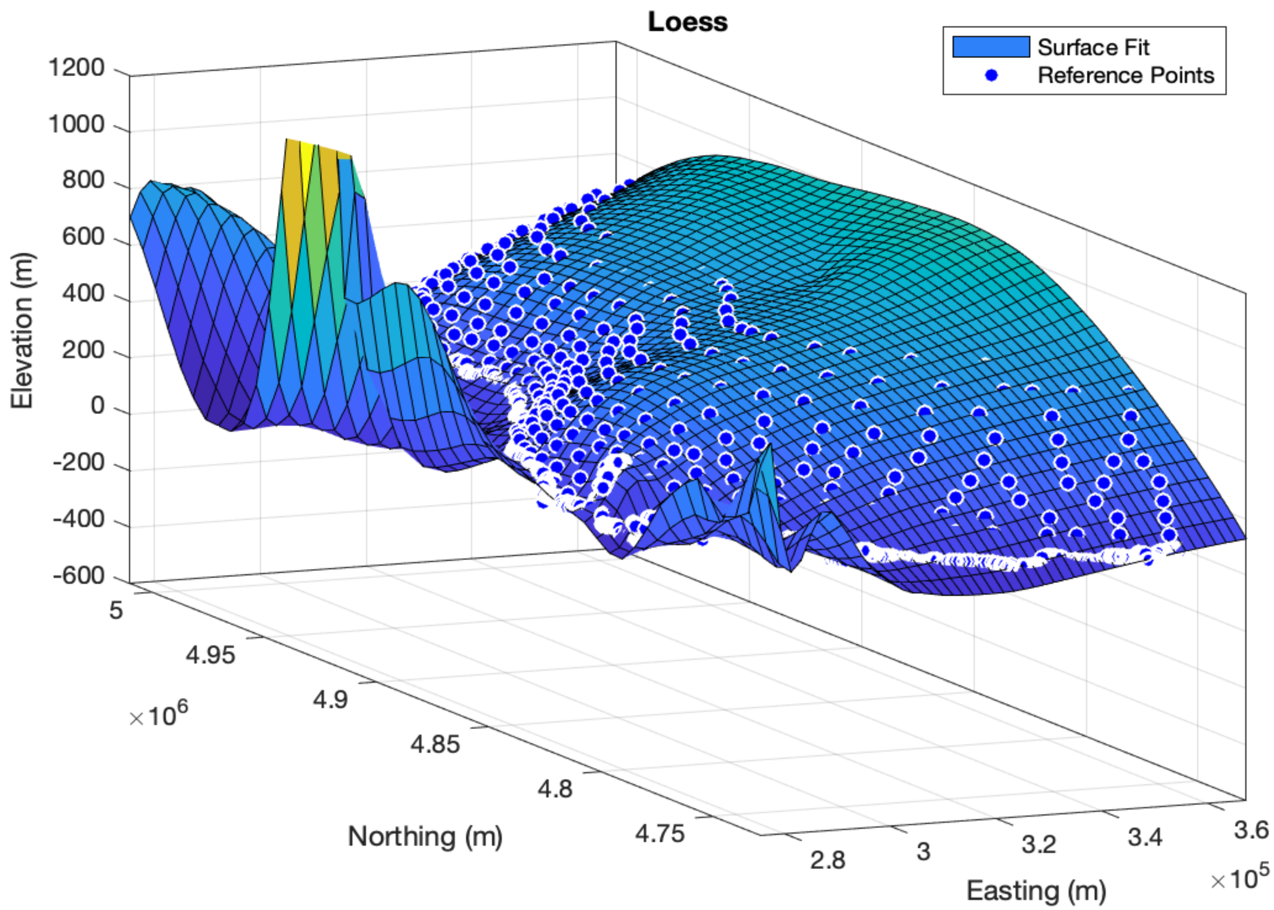

Figure A5. Local quadratic regression method ice-surface fit. Reference points correspond to the equal-elevation lines from Clark 1992. Viewpoint is looking Northeast in the up-ice direction.

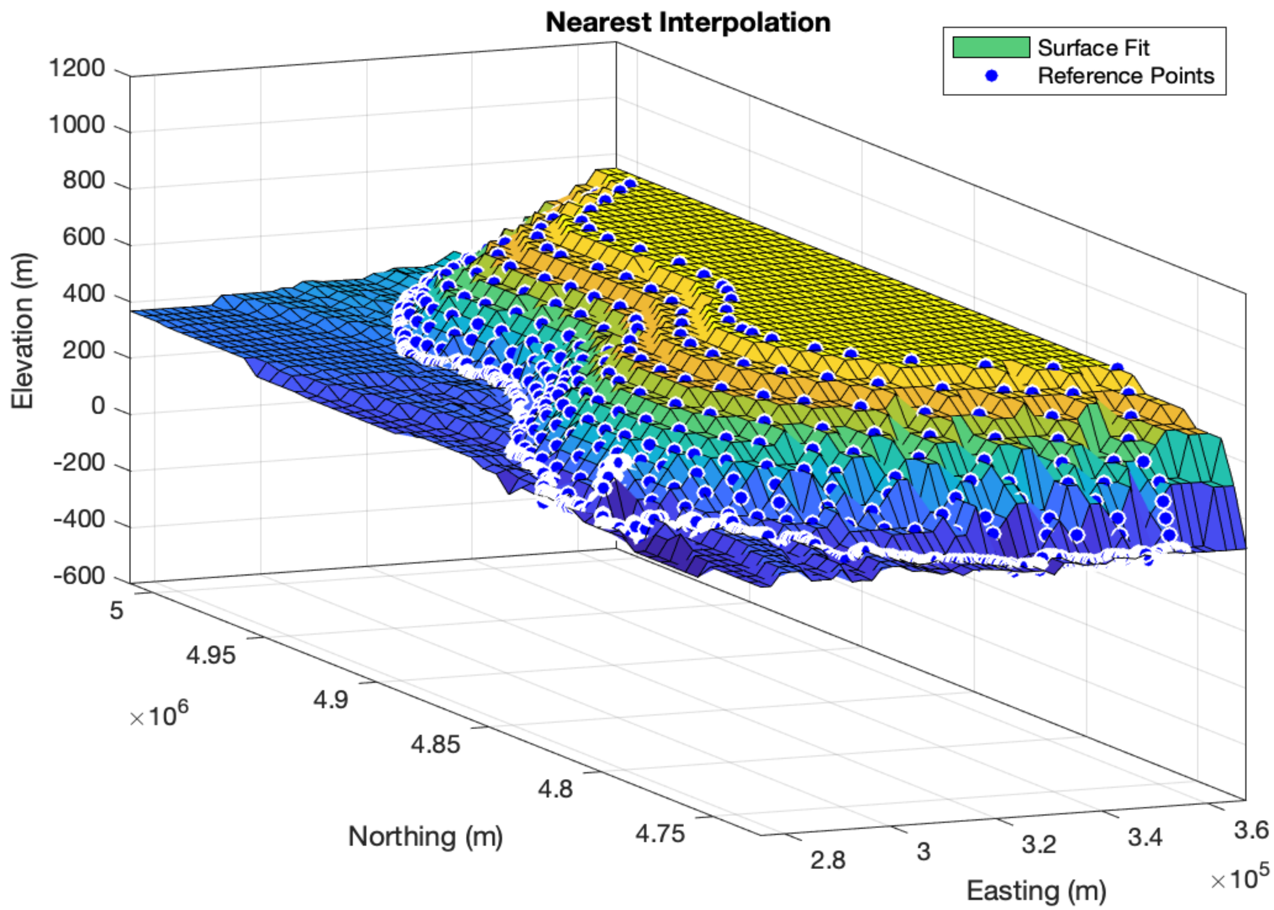

Figure A6. Nearest neighbor interpolation method ice-surface fit. Reference points correspond to the equal-elevation lines from Clark 1992. Viewpoint is looking Northeast in the up-ice direction.